Incipient motion of shells and shell fragments

by

Christophe Nicolas Aimé Troch

Thesis presented in partial fulfilment of the requirements for the degree
Masters of Science in Applied Mathematics at the
Stellenbosch University

Supervisor: Prof. G.J.F. Smit
Co-supervisor: Dr. G.P.J. Diedericks
Faculty of Science
Department of Mathematical Sciences

December 2015

Declaration

By submitting this thesis electronically, I declare that the entirety of the work contained therein is my own, original work, that I am the sole author thereof (save to the extent explicitly otherwise stated), that reproduction and publication thereof by Stellenbosch University will not infringe any third party rights and that I have not previously in its entirety or in part submitted it for obtaining any qualification.

December 2015

Abstract

In the present study, the erosion characteristics of shells and shell fragments are investigated. When shells settle, they settle like leaves, where the biggest cross section is exposed to the drag, unlike when they are flat on the bed, where the smaller cross section is exposed to the direction of flow. The settling velocity of shells is thus lower than the velocity required to make them erode. A model is presented to determine the critical bed shear stress of various shells at incipient motion lying flat on a horizontal sand bed. This model makes use of the hydrodynamical forces, where drag and lift forces are taken into consideration. The mussel and limpet shells are investigated, as well as various shapes of fossilized shells and fragments, in their dirty and clean states. These results are compared to results found in literature. Experiments were conducted in an open channel to determine critical bed shear stresses for incipient motion of the shells using Vanoni's side-wall correction. The lift and drag forces of the mussel and limpet shells are also determined under the flow of water using a strain gauge. The experimental data is compared to the data obtained by the analytical model. The Shields parameter is used in an attempt to relate the erosion characteristics of the shells to non-uniform sand grains on a bed.

Opsomming

In hierdie studie word die erosie kenmerke van skulpe en skulp fragmente ondersoek. Wanneer skulpe afsak na die bodem, word, soortgelyk soos blare rangskik onder 'n boom, die grootste deursnit area van die skulp aan die sleurkrag blootgestel, in teenstelling met wanneer dit op die bodem lê, waar die kleiner deursnit area blootgestel is aan die vloei. Die sinksnelheid van skulpe is dus laer as die snelheid wat vereis word om hulle te laat erodeer. 'n Model om die kritieke skuifspanning vir die aanvang van beweging van verskeie skulpe wat op 'n horisontale sandbodem lê te bepaal, word voorgestel. Hierdie model maak van die hidrodinamiese kragte, waar die sleurkrag en hefkrag in ag geneem word, gebruik. Mossel- en klipmosselskulpe word ondersoek, asook verskillende vorms van gefossiliseerde skulpe en fragmente van skulpe, in hulle vuil en skoon toestande. Hierdie resultate word dan met resultate soos gevind in literatuur vergelyking. Eksperimente om die kritiese skuifspanningskragte op die bodem te bepaal vir die aanvangsbeweging van die skulpe word in 'n oop kanaal gedoen deur van Vanoni se wandmuur regstelling gebruik te maak. Die sleurkragte en hefkragte van die mossel en klipmossel skulpe word onder die invloed van vloeiende water met behulp van 'n vervormingsmeter bepaal. Die eksperimentele data word met die data wat verkry is deur die analitiese model vergelyking. Die Shield parameter word gebruik in 'n poging om die erosie kenmerke van die skulpe met nie-uniforme sandkorrels wat op die bodem lê te vergelyk.

Acknowledgements

I would like to express thanks to the individuals and organizations that helped me both in my research and the development of this thesis. First and foremost, I would like to thank my supervisor, Prof. G.J.F. Smit, and co-supervisor Dr. G.P.J. Diedericks, for the opportunity to do this project. I would further like to thank Christiaan Visser from the Civil Engineering Department of the University of Stellenbosch that made a Lab available for experiments. I would like to express my gratitude to Johan Kieviet from the CSIR for supplying the equipment needed as well as the time he spent on guidance for operating it. I would further like to thank the National Research Fund for the necessary funds that helped me to complete this project.

Christophe Nicolas Aimé Troch

Notation

A	flow area of channel	$[m^2]$
A_p	frontal area of shell	$[m^2]$
A_s	base area of shell	$[m^2]$
a	length of shell	$[m]$
a_b	length of parallelogram base	$[m]$
b	breadth of shell	$[m]$
B	breadth of channel	$[m]$
c	height of shell	$[m]$
β	shape parameter	$[-]$
C_d	discharge coefficient	$[-]$
C_D	drag coefficient	$[-]$
C_L	lift coefficient	$[-]$
d	grain diameter	$[m]$
D_{50}	characteristic diameter	$[m]$
D_h	hydraulic diameter	$[m]$
d_n	nominal diameter	$[m]$
d_s	area diameter	$[m]$
f	friction factor	$[-]$
F_D	drag force	$[N]$
F_G	downwards force	$[N]$
F_L	lift force	$[N]$
F_s	static coulomb friction force	$[N]$
Fr	Froude number	$[-]$
g	gravitational acceleration	$[m.s^{-2}]$

h	depth of flow	$[m]$
H	total head	$[m]$
k_s	equivalent grain roughness	$[m]$
K	von Karman constant	$[-]$
l	mixing length	$[m]$
L	characteristic length	$[-]$
l_c	chord length	$[m]$
m	mass of shell	$[kg]$
N	normal force	$[N]$
P	wetted perimeter	$[m]$
ρ_w	density of water	$[kg.m^{-3}]$
ρ_s	density of shell	$[kg.m^{-3}]$
ρ_f	density of fossilized shell	$[kg.m^{-3}]$
Q	discharge	$[m^3.s^{-1}]$
R	radius of circle	$[m]$
Re	Reynolds number	$[-]$
R_h	hydraulic radius	$[m]$
S	total surface area of shell	$[m^{-2}]$
S_E	energy slope	$[-]$
SF	Corey shape factor	$[-]$
t_c	thickness of shell	$[m]$
t	time	$[s]$
τ_b	bed shear stress	$[kg.m^{-1}.s^{-2}]$
τ_w	wall shear stress	$[kg.m^{-1}.s^{-2}]$
τ_t	total shear stress	$[kg.m^{-1}.s^{-2}]$
u	velocity	$[m.s^{-1}]$
U	average velocity	$[m.s^{-1}]$
U_m	mean velocity	$[m.s^{-1}]$
u_*	shear/friction velocity	$[-]$
u_c	static coulomb friction factor	$[-]$
ν	kinematic viscosity of water	$[m^2.s]$
V	total volume of shell	$[m^3]$
x	x-axis of channel	$[-]$

y	y-axis of channel	$[-]$
z	z-axis of channel	$[-]$
y_0	zero velocity level	$[m]$
y_h	hydraulic depth	$[m^3]$
θ	Shields parameter	$[-]$
Θ	angle of the weir	$[^\circ]$
ϕ	angle of friction	$[^\circ]$

Contents

Chapter 1

Introduction

1.1 Preface

Tidal currents, wind-driven currents, and the orbital motion of surface waves are some of the forces at the seabed that cause ocean sediment to move [1]. The shear stresses caused by these phenomena, if strong enough, affect the geology and habitat of the seafloor through their influence on sediment texture. For example, finer grained sediments such as mud are located in areas of low stress, whereas coarser sediments such as sand and gravel are typically found in areas of high stress. This is a result of finer material being re-suspended and swept away in areas of high stress [2].

The aim of this study is to determine under which conditions sediment such as shells and shell fragments on the ocean floor start to move. Existing knowledge and data of shells being transported as sediment is minimal, whereas the motion of sediments such as sand, gravel, silts and clay have been extensively researched. This is partly due to the irregular shapes of shells that make determining the movement of shells under the action of flow complicated [3]. The shape of shells is more disc-shaped when compared to spherical shape of sand which causes a settling velocity that is lower than an equivalent sand particle, but a higher erosion velocity.

In order for sediment on the seafloor to move, incipient motion must be reached. The term incipient motion refers to the bed shear stress induced by the flow at which sediment

begin to move. Incipient motion thus refers to the critical bed shear stress that must be exceeded [4]. The incipient motion, and thus also erosion of shells and shell fragments differs drastically from that of equivalent size sand particles. According to Ramsdell et al. [5], this is because shells settle in the same way that leaves settle on the ground under a tree. Thus only a small cross-sectional area of the shell is exposed to the horizontal direction of the flow compared to the weight of the shell. This characteristic makes shells difficult to erode. Another characteristic of shells is that they have a small settling velocity due to their large cross-sectional area. This implies that shells are always visible on top of the sand and consequently also shield the finer, more easily eroded sediment such as sand [5]. This can be seen in Figure 1.1 where a layer of mussel shells, approximately 10 centimeters thick, is covering the sand on a beach.

Figure 1.1. Blue mussel shells visible on top of the sand as seen at Yzerfontein on the West Coast of South Africa.

In this study, critical bed shear stresses are investigated for shells under unidirectional flow of water over different horizontal surfaces and shell placements. Laboratory experiments in an open channel are conducted to investigate the incipient motion under flowing water of various sea shells. Particular focus is placed on the Patellogastropoda, commonly known as the Limpet shell, and the Mytilus galloprovincialis, commonly known as the Blue mussel. These shells dominate nearly 2000 kilometers of the South African shoreline. Fossilized shells and shell fragments mined off the coast near Walvis Bay will also be considered. The incipient or threshold motion of these shells under flowing water is then used to define their underwater transport properties.

1.2 Background to this study

The topic of this project originated mainly because of a phosphate harvesting project off the coast of Namibia near to Walvis Bay. Phosphate is used as fertilizer. This project involved an investigation into feasibility of dredging underground sediment from the ocean floor from sea vessels. This sediment mainly consisted of fossilized shells and phosphate. The phosphate had to be removed from the shells and the shells had to be discarded. The question then arose as to where to discard these shells. If shells were to be dumped in coastal regions, it is important to know how the shells would be distributed by the flow of the sea to minimize ecological damage. For the shells to be processed on the dredger and thrown back into the ocean on site, the transport properties of the shells must be known, for it is important to know under which flow velocity these shells will be swept away, otherwise the same shells will be pumped from the ocean floor that contain no phosphate. The same types of questions arise for the use of shells in coastal restoration and beach nourishment projects where shells are distributed over sandy areas to protect the sand against erosion.

Dey [3] presented a model to determine the critical bed shear stress at incipient motion for bivalve shells, namely Coquina Clam, Cross-barred Chione and Ponderous Ark, on a horizontal bed under a unidirectional flow of water. These shells were tested experimentally for the condition of incipient motion. A similar methodology is used for the shells in this study, which includes the Blue Mussel, Limpet and various fossilized shell and shell fragments, to determine values of the critical bed shear stresses.

Ramsdell et. al. [5] presented a method to relate the incipient motion properties of the shells investigated by Dey [3] into Shields parameters. The Shields parameter is quantified for shells in this study and related to the corresponding Shields parameter of sand grains .

1.3 Overview of this study

In Chapter 2 an overview of the factors controlling the movement of sediment is given. These factors include the different type of sediment transport as well as how frictional and shear forces affects the movement of sediment. The shells investigated is this study are irregular in shape, a shape parameter is defined and applied to the shells in Chapter 3 in an attempt to correlate the flow behavior with that of the shape parameter. The shape parameter that is defined makes use of the Corey shape factor.

Experimental tests were done to determine critical bed shear stresses of the shell and shell fragments. These tests were done in an open channel. Chapter 4 is devoted to the open-channel and the hydrodynamic laws thereof. This includes the type and states of flow, the velocity distribution as well as flow resistance of the channel and how sidewall correction is applied for the boundaries of the channel under consideration. The equations for solving the friction factors and bed shear stresses are then deduced.

Chapter 5 explains the experimental setup as well as the methodology used to record the necessary measurements to calculate average flow velocity at which incipient motion occurs on two bed surfaces of different roughness. A strain gauge is also used to determine the drag and lift forces of the mussel and limpet shell. The average flow velocity is then used to determine critical bed shear stresses using the equations derived in Chapter 4.

The analytical model to determine the critical bed shear stress for each shell is derived in Chapter 6. This model uses the forces on a shell at the critical stage. This includes the force due to gravitation, drag and lift force, as well as the friction between the bed and the shell. Equations for calculating the mean velocity received by each different type of shell is deduced using a logarithmic velocity profile distribution as derived in Chapter 4. The mean velocities of the mussel and limpet shells are then used to determine their

drag and lift coefficients. These results are then used to determine the critical bed shear stress of each shell species on each bed surface in Chapter 7. The analytical results are then compared to those of the experimental results. The shape parameter of each shell is also compared to critical bed shear stress of each shell in an attempt to find a relationship between the shape parameter and the incipient motion of the shells.

Chapter 8 relates the shells to the Shields parameter, this is done by relating the thickness of the shell to that of the diameter of a sand grain. A non-uniform particle distribution plot is also used to derive a Shields parameter for the shells. Ratios between these Shields parameter values exists and are discussed.

Chapter 2

Background

This chapter looks at the physical conditions which lead to the erosion, transport and deposition of sediment. The sediment transport and deposition processes are valid anywhere where moving water is present, which includes estuaries, beaches as well as the deep ocean [2].

2.1 Factors controlling the movement of sediment

When water flows over the bottom of a sediment surface, and the flow is strong enough, particles can be picked up by the flow force and transported. These particles are again deposited when the speed of the flow diminishes. Not all particles are lifted up in suspension by the flow and particles that are too large to be lifted are rolled and bounced along the bottom surface. Thus, one of the most important parameters controlling the transport and deposition of sediment particles is grain size [2]. The four modes of particle transport in water are sliding, rolling, saltation and suspension:

- **Sliding:** Particles that slide stay in continuous contact with the surface, merely tilting as they move.
- **Rolling:** Rolling grains also stay in continuous contact with the surface, only rolling as they move.
- **Saltation:** Saltating particles 'jump' along the bed in a series of low trajectories.

- **Suspension:** Particles in suspension follow long and irregular paths within the water and seldom come in contact with the bed.

2.2 Bedload and suspended load

Sediment particles in the Sliding, Rolling and Saltation categories collectively form the bedload, whereas the suspended load consists of the particles in the Suspension category as illustrated in Figure 2.1.

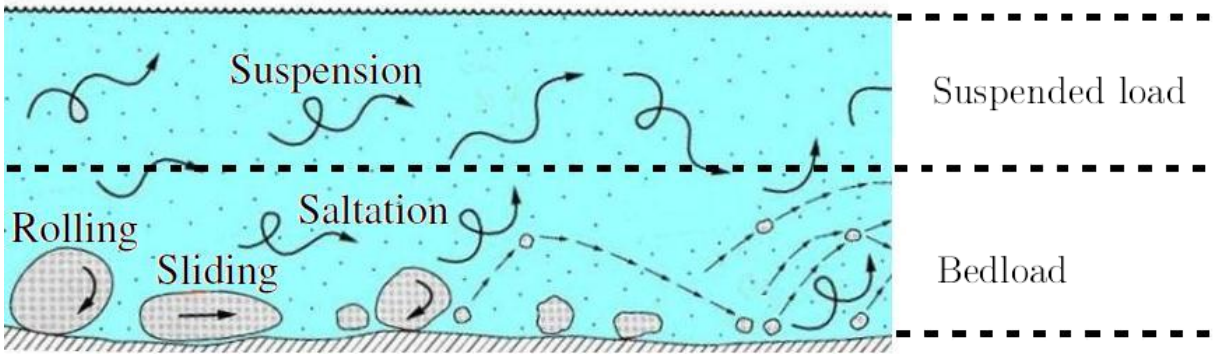

Figure 2.1. Bedload and suspended load.

Sliding and rolling particles are prevalent in slower flows whereas saltating and suspended particles are prevalent in faster flows [2]. The key aspect of this study is to determine when shells and shell fragments start to move and focus will thus only be placed on the modes of transport which include sliding and rolling of particles since they occur at lower velocities than saltation and suspended particles.

2.3 Frictional forces and the boundary layer

If a fluid flows over a solid boundary, the surface has a retarding effect on the velocity of the fluid. The region of flow affected by the bottom surface is called the boundary layer. In this boundary layer, the fluid velocity gradually increases with distance from the bottom boundary known as the bed. Given that no sediment on the bed is moving, in theory, the layer directly in contact with this bed should be zero [2]. A velocity gradient thus exists

and the gradient is in the perpendicular direction from the bed. This velocity gradient for the necessary conditions to this study, is described more thoroughly in Section 4.4.

If the layers of fluid above the bottom surface are moving, the successive layers of water moving over each other has a frictional force due to the layer above it. This frictional force tends to drag it along, while the frictional force from the layer below, tends to drag it back. These forces are known as shear stresses. To determine whether sediment at the bed will move, the value of this shear stress must be determined at the bed. This is known as the bed shear stress τ_b. When this bed shear stress τ_b becomes strong enough to overcome the frictional and gravitational forces holding the shells on the bed, the force is known as the critical bed shear stress [2].

Chapter 3

Shape parameters

Most particles of practical interest are irregular in shape, such as the shape of gravel and shells. A variety of empirical factors have been proposed to describe non-spherical particles and correlate then with their flow behaviour.

3.1 The Corey shape factor

One way of characterizing the shape of an irregular particle is in terms of the lengths a, b and c of the major, intermediate, and minor axes, as expressed by the Corey shape factor [6]. These axes are illustrated in Figure 3.1 for a shell shaped particle.

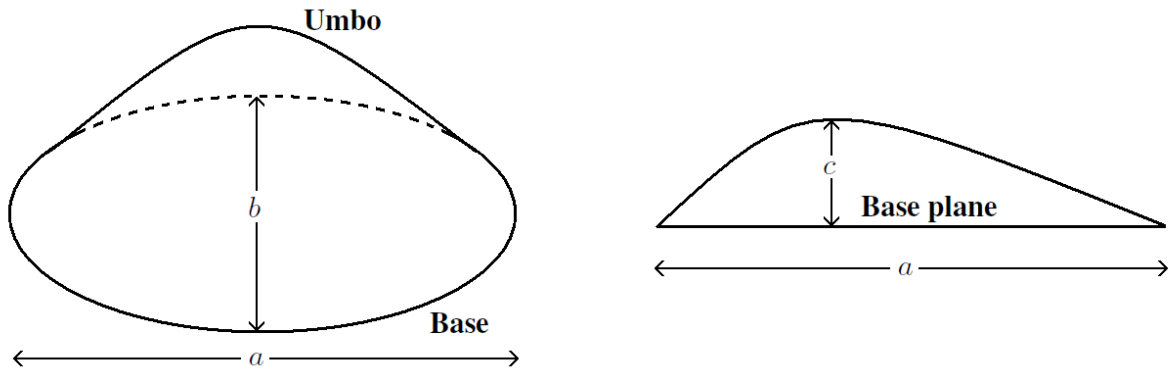

Figure 3.1. The major, intermediate, and minor axes for a shell shaped particle.

The Corey shape factor is defined as follows:

$$SF = \frac{c}{\sqrt{ab}}, \tag{3.1}$$

where SF is the Corey shape factor and the length, breadth and height of the object is given by a, b, and c respectively. The Zingg diagram, shown in Figure 3.2, is widely used by researchers to graphically represent and classify pebble shapes. Zingg proposed a Cartesian coordinate system with $\frac{c}{b}$ and $\frac{b}{a}$ as indices for the shape diagram. The proportion $\frac{c}{b}$ is a measure of the flatness and the proportion $\frac{b}{a}$ is a measure of the elongation of the particle [7].

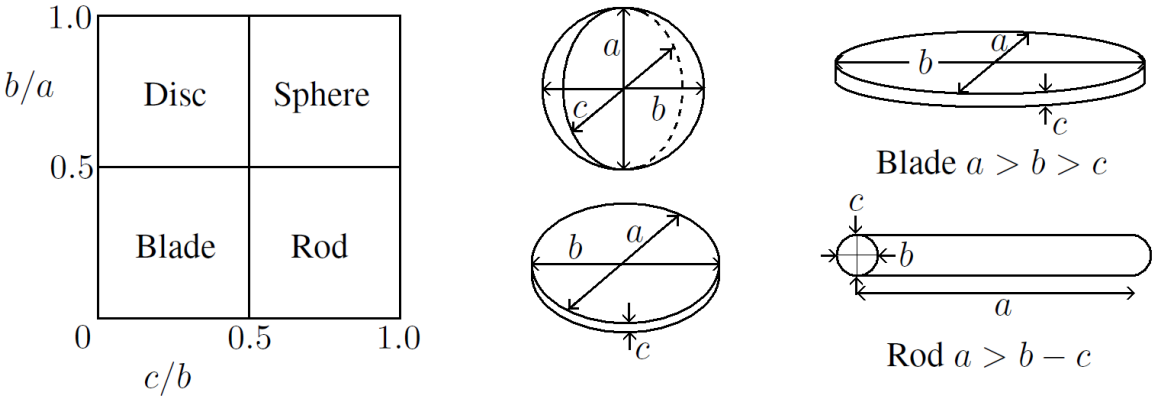

Figure 3.2. The Zingg diagram.

This shape factor does not account for surface and volume distributions of the particle. The drawback of not accounting for the surface and volume distributions is that objects with the same shape factors SF could have different hydrodynamic characteristics. For example, a sphere and a cube have the same shape factor $SF = 1$, as seen in the Zingg diagram, but the drag and lift forces of a sphere and a cube differ significantly.

3.2 The shape parameter

Alger and Simons [8] proposed the following shape parameter to account for the surface and volume distributions:

$$\beta = (SF)\frac{d_s}{d_n}, \tag{3.2}$$

where SF is the Corey shape factor, given by equation (3.1), d_s and d_n are referred to as the area and the nominal diameters, respectively. The area diameter d_s, is the diameter of a sphere that has the same surface area as the particle. The nominal diameter d_n is the diameter of a sphere that has the same volume as the particle. These are defined as:

$$d_s = \left(\frac{S}{\pi}\right)^{\frac{1}{2}} \tag{3.3}$$

and

$$d_n = \left(\frac{6V}{\pi}\right)^{\frac{1}{3}}, \tag{3.4}$$

where S is the total surface area and V is the total volume of the shell. To calculate the total surface area S of the shells in this study, the base area A_s is firstly determined by using the pixels from digital images of the shells. This is done by photographing each sample shell on a uniform coloured surface, with the camera steadily mounted on a tripod such that each image of each shell is captured at equal distance and perpendicular to the surface that the shell is placed on. A ruler is positioned next to each shell to calculate the relationship between the true length and the number of pixels in each image. The ruler is then removed and without the camera or shell being adjusted or moved from the previous photograph taken, another photograph is taken of each shell. By using digital processing techniques, all the non-white pixels in the images are changed to the colour black, as is illustrated in Figure 3.3 and Figure 3.4 for a mussel shell sample, and in Figure 3.5 and Figure 3.6 for a limpet shell sample.

The black pixels in the processed images are then summed. By calculating the scale between the pixels and the true length on the ruler, a true length can be assigned as well as an area for a pixel in the image. The area of each shell is then calculated as the total sum of these black pixels found inside the borders of a shell. This procedure is done for each of the mussel and limpet shells, as well as for the fossil shell and fossil shell fragment samples.

The length a, breadth b and height c of each of the shells used in this study was measured using a typical Vernier caliper and the thickness t_c of the shell was measured with a thickness caliper. The density of the shells were determined as explained in Chapter 5.

Figure 3.3. The original mussel shell image.

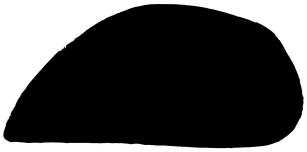

Figure 3.4. The processed mussel shell image.

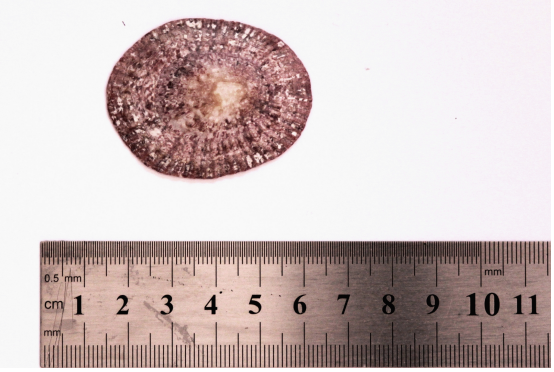

Figure 3.5. The original limpet shell image.

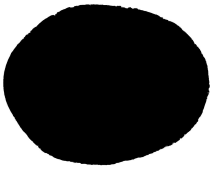

Figure 3.6. The processed limpet shell image.

The mussel and limpet shells have a density of $\rho_s = 2586$ kg.m^{-3}, and the fossilized shells have a density of $\rho_f = 2614$ kg.m^{-3}. By knowing the densities of the different shell samples, the volume of each of the samples is calculated. This is done by knowing that $V = \frac{m}{\rho}$, where m is the mass of the shell that is weighed on a scale and ρ is the density of the sample under consideration. The base area A_s, the length a, breadth b, height c, thickness t_c, mass m and volume V of the shells as estimated by the above methods are summarized in Tables 3.1 to 3.3.

The total surface area S was determined next. For the mussel, limpet, fossilized clam and shell fragments, it is assumed that the total surface areas of the top and bottom sides of the shells are equal. By using this assumption, the total surface area S of a shell can be calculated by knowing that $V = \frac{St_c}{2}$, where the $\frac{1}{2}$ factor is introduced to account for the top and bottom areas of the shell. The total surface areas S of the non bivalve shells was determined by approximating the shape of the shell by a known three-dimensional geometric shape, such as a cylinder or a cone. The shape factor SF was then determined from equation (3.1). The area diameter d_s and the nominal diameter d_n were then calculated from equations (3.3) and (3.4). Consequently, the shape parameter β was calculated from equation (3.2). The total surface area, shape factor, area diameter, nominal diameter and the new shape parameters for each of the sample shells are summarized in Tables 3.4 and 3.5. The various shells that are investigated in this study are shown in Figure 3.7.

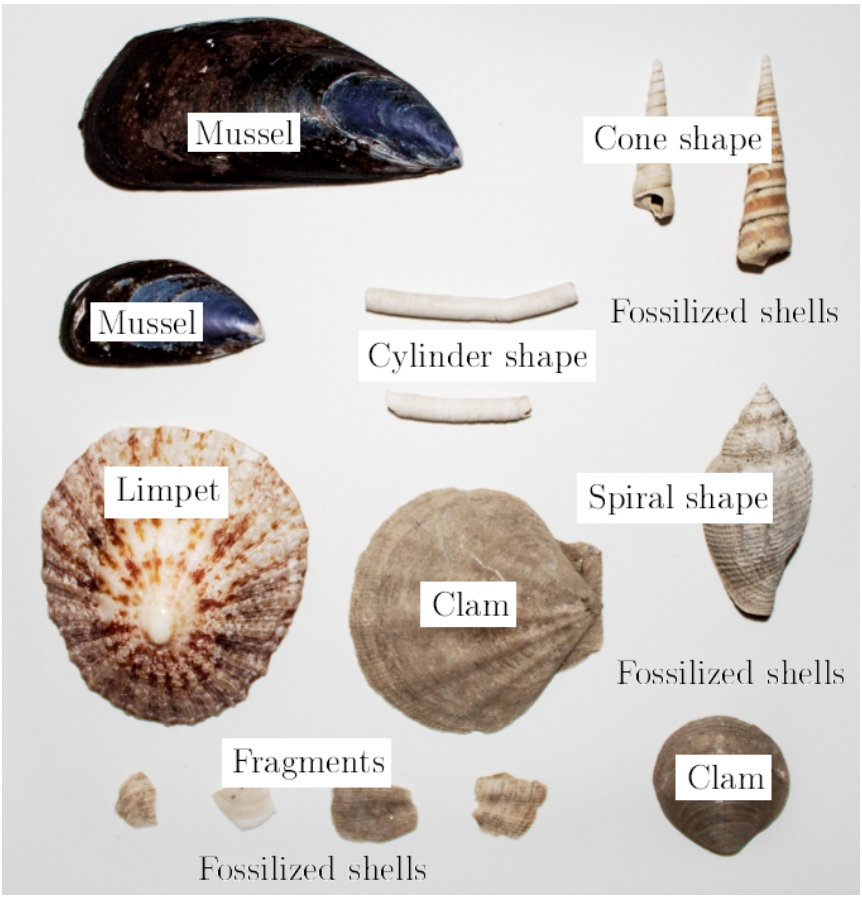

Figure 3.7. Examples of the shells used in this study.

Table 3.1. Characteristics of the mussel and limpet sample shells.

Shell Sample	a (cm)	b (cm)	c (cm)	t_c (cm)	A_s (cm^2)	mass (g)	Volume (cm^3)
Mussel 1	8.20	3.80	1.20	0.100	23.53	7.7	2.841
Mussel 2	7.95	3.70	1.10	0.100	22.11	7.6	2.804
Mussel 3	7.80	3.60	1.10	0.100	21.55	7.5	2.768
Mussel 4	8.00	3.50	1.05	0.095	20.61	5.6	2.066
Mussel 5	7.55	3.60	1.05	0.100	19.96	6.3	2.325
Mussel 6	8.00	3.80	1.10	0.100	22.75	7.4	2.731
Mussel 7	7.40	3.70	1.10	0.095	20.52	6.2	2.288
Mussel 8	6.95	3.20	0.95	0.090	17.34	4.8	1.771
Mussel 9	6.90	3.10	0.95	0.090	16.18	3.9	1.439
Mussel 10	6.60	3.10	1.00	0.090	15.30	4.5	1.661
Mussel 11	6.20	3.00	0.95	0.090	14.30	3.6	1.328
Mussel 12	6.45	3.00	0.95	0.090	14.67	3.6	1.328
Mussel 13	6.30	2.95	0.90	0.080	13.92	3.1	1.144
Mussel 14	6.10	3.20	0.95	0.090	14.47	4	1.476
Mussel 15	6.60	3.20	0.90	0.090	15.84	3.8	1.402
Mussel 16	6.05	2.80	0.95	0.090	12.71	3.9	1.439
Mussel 17	5.75	2.80	0.90	0.080	12.48	3	1.107
Mussel 18	5.30	2.55	0.80	0.070	10.16	2	0.738
Mussel 19	5.30	2.40	0.80	0.080	9.83	2.1	0.775
Mussel 20	5.20	2.50	0.70	0.070	10.07	2.1	0.775
Mussel 21	5.10	2.40	0.75	0.060	9.39	2.2	0.812
Mussel 22	4.90	2.40	0.80	0.060	8.75	2	0.738
Mussel 23	4.80	2.35	0.70	0.060	8.36	1.5	0.554
Mussel 24	4.50	2.30	0.70	0.060	8.09	1.9	0.701
Mussel 25	4.60	2.40	0.70	0.060	8.35	1.6	0.590
Mussel 26	11.50	5.40	2.00	0.190	49.21	27.5	10.148
Mussel 27	4.80	2.40	0.80	0.060	8.54	2	0.738
Mussel 28	4.95	2.45	0.80	0.060	9.00	2.3	0.849
Mussel 29	8.60	3.90	1.20	0.110	25.09	9.8	3.616
Mussel 30	6.80	3.30	1.00	0.100	17.04	5.1	1.882
Mussel 31	7.35	3.50	1.10	0.095	19.14	5.5	2.030
Mussel 32	7.40	3.65	1.00	0.105	19.22	6.8	2.509
Limpet 1	6.50	5.85	2.10	0.200	29.89	18.8	6.937
Limpet 2	5.40	4.40	1.10	0.120	18.05	6.7	2.472
Limpet 3	4.70	3.70	1.30	0.120	13.45	4.7	1.734
Limpet 4	3.50	3.20	0.90	0.100	8.89	2.4	0.886
Limpet 5	2.30	1.82	0.55	0.055	3.21	0.5	0.185

Table 3.2. Characteristics of the fossilized clam and shell fragment samples.

Shell Sample	a (cm)	b (cm)	c (cm)	t_c (cm)	A_s (cm^2)	mass (g)	Volume (cm^3)
Clam 1	4.80	4.80	0.90	0.15	17.09	7.18	2.75
Clam 2	5.40	5.40	0.90	0.13	22.35	7.46	2.85
Clam 3	4.00	4.00	0.65	0.1	11.76	2.72	1.04
Clam 4	3.00	3.00	0.90	0.15	6.74	2.67	1.02
Clam 5	2.90	2.90	0.65	0.1	6.41	0.84	0.32
Fragment 1	1.20	1.20	0.20	0.1	1.13	0.23	0.09
Fragment 2	1.25	1.25	0.20	0.05	1.24	0.12	0.04
Fragment 3	1.26	1.26	0.10	0.02	1.26	0.04	0.02
Fragment 4	1.87	1.87	0.20	0.05	2.74	0.39	0.15
Fragment 5	1.63	1.63	0.25	0.1	2.09	0.29	0.11
Fragment 6	1.63	1.63	0.10	0.02	2.09	0.14	0.05

Table 3.3. Characteristics of the fossilized non bivalve shell samples.

Shell Sample	a (cm)	b (cm)	c (cm)	A_s (cm^2)	mass (g)	Volume (cm^3)
Twirl 1	4.95	2.2	2.2	6.55	5.13	6.30
Twirl 2	4.7	2.2	2.2	5.17	3.26	5.60
Twirl 3	4.4	1.4	1.4	3.08	2.06	2.30
Cone 1	3.8	1.4	1.4	2.66	2.82	3.14
Cone 2	4.2	1.2	1.2	2.52	1.36	1.86
Cone 3	3.3	0.9	0.9	1.49	0.90	0.89
Cylinder 1	6.3	0.45	0.45	2.84	0.89	1.00
Cylinder 2	4.55	0.5	0.5	2.28	0.85	0.89
Cylinder 3	3	0.5	0.5	1.50	0.48	0.59

Table 3.4. The shape factor β of the mussel and limpet sample shells.

Shell Sample	S (cm^2)	d_s (cm)	d_n (cm)	β
Mussel 1	56.83	4.25	1.76	0.52
Mussel 2	56.09	4.23	1.75	0.49
Mussel 3	55.35	4.20	1.74	0.50
Mussel 4	43.50	3.72	1.58	0.47
Mussel 5	46.49	3.85	1.64	0.47
Mussel 6	54.61	4.17	1.73	0.48
Mussel 7	48.16	3.92	1.63	0.50
Mussel 8	39.36	3.54	1.50	0.47
Mussel 9	31.98	3.19	1.40	0.47
Mussel 10	36.90	3.43	1.47	0.52
Mussel 11	29.52	3.07	1.36	0.50
Mussel 12	29.52	3.07	1.36	0.49
Mussel 13	28.60	3.02	1.30	0.49
Mussel 14	32.80	3.23	1.41	0.49
Mussel 15	31.16	3.15	1.39	0.44
Mussel 16	31.98	3.19	1.40	0.53
Mussel 17	27.68	2.97	1.28	0.52
Mussel 18	21.09	2.59	1.12	0.50
Mussel 19	19.37	2.48	1.14	0.49
Mussel 20	22.14	2.65	1.14	0.45
Mussel 21	27.06	2.93	1.16	0.54
Mussel 22	24.60	2.80	1.12	0.58
Mussel 23	18.45	2.42	1.02	0.50
Mussel 24	23.37	2.73	1.10	0.54
Mussel 25	19.68	2.50	1.04	0.51
Mussel 26	106.82	5.83	2.69	0.55
Mussel 27	24.60	2.80	1.12	0.59
Mussel 28	28.29	3.00	1.17	0.59
Mussel 29	65.75	4.57	1.90	0.50
Mussel 30	37.64	3.46	1.53	0.48
Mussel 31	42.73	3.69	1.57	0.51
Mussel 32	47.79	3.90	1.69	0.45
Limpet 1	69.37	4.70	2.37	0.68
Limpet 2	41.21	3.62	1.68	0.49
Limpet 3	28.91	3.03	1.49	0.63
Limpet 4	17.71	2.37	1.19	0.54
Limpet 5	6.71	1.46	0.71	0.56

Table 3.5. The shape factor β of the fossilized sample shells and fragments.

Shell Sample	S (cm^2)	d_s (cm)	d_n (cm)	β
Clam 1	36.65	3.42	1.74	0.37
Clam 2	44.90	3.78	1.76	0.36
Clam 3	24.80	2.81	1.26	0.36
Clam 4	14.61	2.16	1.25	0.52
Clam 5	13.44	2.07	0.85	0.55
Twirl 1	18.74	2.44	2.29	0.71
Twirl 2	18.12	2.40	2.20	0.75
Twirl 3	10.18	1.80	1.64	0.62
Cone 1	13.83	2.10	1.82	0.70
Cone 2	10.33	1.81	1.52	0.64
Cone 3	6.40	1.43	1.19	0.62
Cylinder 1	9.22	1.71	1.24	0.37
Cylinder 2	7.54	1.55	1.19	0.43
Cylinder 3	5.11	1.27	1.04	0.50
Fragment 1	2.77	0.94	0.55	0.28
Fragment 2	2.80	0.94	0.44	0.34
Fragment 3	2.58	0.91	0.31	0.23
Fragment 4	5.99	1.38	0.66	0.22
Fragment 5	4.19	1.15	0.59	0.30
Fragment 6	5.19	1.29	0.46	0.17

Chapter 4

Flow in an open-channel

In this study, experimental tests were done in an open channel. Understanding the hydrodynamic laws of flow in an open channel is necessary and is explained in this chapter. Open-channel flow is flow within a conduit with a free surface, known as a channel.

4.1 Definitions for the open-channel

The coordinate system applied in this chapter is shown in Figure 4.1. The flow area of the open-channel is given by $A = Bh$, where B is the width of the channel and h is the flow depth as measured from the bottom of the channel to the water surface. The wetted perimeter is given by [9]:

$$P = B + 2h, \tag{4.1}$$

and the hydraulic radius is defined as:

$$R_h = \frac{A}{P}. \tag{4.2}$$

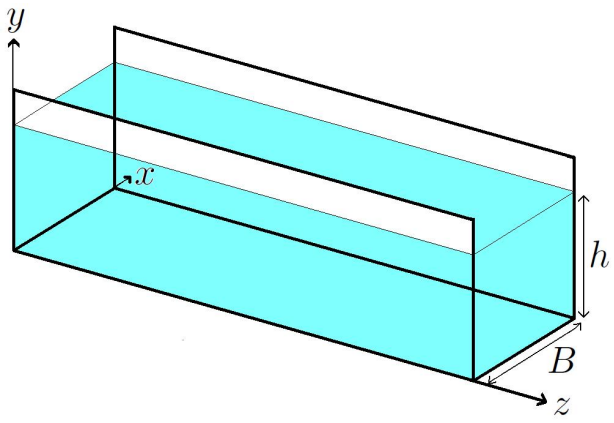

Figure 4.1. The open-channel.

4.2 Types of flow

Flow in an open channel is classified into many types and can be described in various ways, as done in the following subsections.

4.2.1 Steady flow and unsteady flow

Steady and unsteady flow is classified on whether the depth and discharge change with time at a point [10]. The flow will be steady if the discharge is constant and the flow depth does not change during the time interval under consideration, thus $\frac{\partial h}{\partial t} = 0$, with h defined in Figure 4.1. Flow is said to be unsteady if the discharge and the flow depth change with time, thus $\frac{\partial h}{\partial t} \neq 0$.

4.2.2 Uniform flow and nonuniform flow

Uniform flow and nonuniform flow is classified on whether the depth varies with distance. The flow is uniform if the depth of flow is the same at every section of the channel, thus $\frac{\partial h}{\partial z} = 0$. Flow is said to be nonuniform if the flow depth does vary with distance, thus $\frac{\partial h}{\partial z} \neq 0$, with directions as defined in Figure 4.1.

4.3 States of flow

The state of flow in an open channel is governed by the effects of viscosity and gravity relative to the inertial forces.

4.3.1 Turbulence of flow

In laminar flow, water particles move in definite smooth streamlines or paths. In turbulent flow, laminar flow paths are twisted into eddies and irregular paths. It means that all particles in the flow system do not follow a fixed or smooth path or streamline. Turbulent flow however still represents a forward motion of the entire flow. Turbulence is usually caused by an increase in flow rate or surface roughness. Chow [9] defines that the flow is turbulent if the viscous forces are weak relative to the inertial forces. This is represented by the Reynolds number and is defined for an open channel as follow:

$$Re = \frac{UD_h}{\nu} = \frac{4UR_h}{\nu}, \tag{4.3}$$

where U is the mean velocity of flow, D_h is the hydraulic diameter, R_h is the hydraulic radius as described in equation (4.2) and ν is the kinematic viscosity of water. The Reynolds number is used to classify the following types of flow in an open channel:

- **Laminar flow** $Re \leq 500$
- **Transitional flow** $500 \leq Re \leq 2000$
- **Turbulent flow** $Re \geq 2000$

The transitional flow is the mixed state between laminar and turbulent states. These ranges are determined from experimental data for open-channel flow.

4.3.2 Effect of gravity

Chow [9] defines that the effect of gravity upon the state of flow is represented by a ratio of inertial forces of the flow to the gravitational forces. This ratio is given by the Froude number which is defined as follow:

$$Fr = \frac{U}{\sqrt{gL}}, \tag{4.4}$$

where U is the mean velocity of flow, g is the acceleration due to gravity and L is the characteristic length. The characteristic length is made equal to the hydraulic depth y_h for open-channel flow. The hydraulic depth is defined as $y_h = AB$, where A is the cross sectional area of the channel and B is the width of the channel as shown in Figure 4.1. The Froude number is used to classify the following types of flow:

- **Subcritical** $Fr < 1$
- **Supercritical flow** $Fr > 1$
- **Critical flow** $Fr = 1$

In the state known as subcritical flow, the role played by gravitational forces are more pronounced such that the flow has low velocity and is described as tranquil and streaming. In the supercritical state, the inertial forces are more dominant, the flow has high velocity and is described as rapid, shooting, and torrential. Critical flow is the state that occurs between the subcritical and supercritical states.

4.4 Velocity distribution

The vertical velocity profile in an open channel is not uniformly distributed. Velocity distribution depends on the roughness and shape of the channel. The velocity profile and the roughness of an open channel is described by means of the friction velocity. Friction velocity is described in the next subsection. For an open channel with a gravel bed and turbulent flow, the velocity profile is assumed to be logarithmically distributed as described by Chow [9].

4.4.1 Classification of flow layers

The flow profile in an open channel can be divided into four layers as described by Liu [11]:

- **Viscous sublayer:** a thin layer just above the bottom of the channel where the flow is laminar, this layer is also referred to as the laminar sublayer
- **Transition layer:** a layer where the viscosity and turbulence are equally important
- **Turbulent logarithmic layer:** turbulent shear stress is constant and equal to bottom shear stress
- **Turbulent outer layer:** velocities are close to constant as a result of eddies that produces mixing of the flow

These flow regions are schematically shown in Figure 4.2.

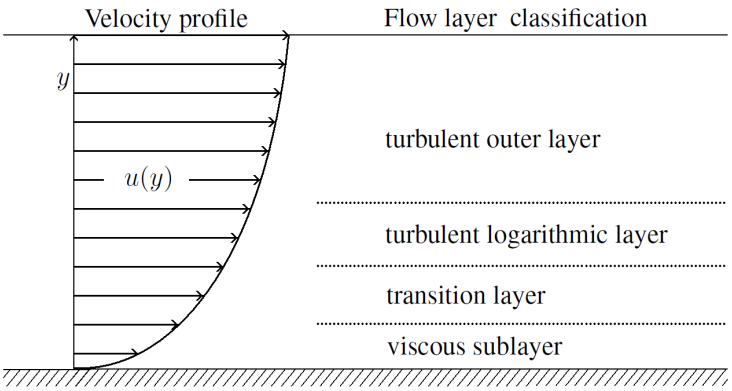

Figure 4.2. Classification of flow regions, layers are not on scale, the turbulent layers account for $80\% - 90\%$ of the region.

4.4.2 Friction velocity u_*

The friction velocity u_* is a measure of the intensity of turbulent eddying, and also the transfer of momentum due to these fluctuations [12]. Liu [11] states that although friction velocity, by definition, has nothing to do with the velocity, it is in fact the fluid velocity at level $y = y_0 e^K$; where y_0 is the zero velocity level of the open channel bed, this level is

discussed further in Section 4.4.4. The constant K is known as the von Karman constant which is a dimensionless constant describing the logarithmic velocity profile of a turbulent fluid flow near the boundary with a no-slip condition. This constant is considered to be universal with a value of $K = 0.41$, which is obtained experimentally in pipe flow [12]. Chow [9] defines the friction velocity as follow:

$$u_* = \sqrt{\frac{\tau_b}{\rho_w}}, \tag{4.5}$$

where τ_b is the bed-shear stress, which is the shear stress at the bed of the channel, and ρ_w is the density of the fluid under consideration.

4.4.3 Concept of surface roughness

The effect of the roughness at the bottom surface on the velocity distribution was first investigated for pipe flow by Nikuradse [9]. He introduced the concept of equivalent grain roughness k_s, also known as the Nikuradse roughness or bed roughness [11]. Based on experimental data, it was found that if the size of the roughness is small enough so that all protrusions are contained within the laminar sub-layer, the bed roughness will not affect the velocity distribution. This type of flow is classified as being hydraulically smooth. The following condition is given for flow to be hydraulically smooth by Schlichting [12]:

$$0 < \frac{u_* k_s}{\nu} < 5. \tag{4.6}$$

When all of the protrusions extend out of the laminar sub-layer, the flow is classified as being hydraulically rough. Thus the bed roughness is large enough that it produces eddies close to the bottom and a viscous sub-layer does not exist. The flow velocity is then not dependent on viscosity. The following condition is given for flow to be hydraulically rough:

$$70 < \frac{u_* k_s}{\nu}. \tag{4.7}$$

When the protrusions extend only partly out of the laminar sub-layer, the flow is in the transitional regime. Thus the velocity distribution is affected by the bed roughness and viscosity. The following condition is given for flow to be in the transitional regime:

$$5 < \frac{u_* k_s}{\nu} < 70. \tag{4.8}$$

4.4.4 Velocity distribution in the turbulent layer

When the turbulent boundary layer is fully developed, the velocity distribution for flow in a uniform channel will become stable. The velocity distribution in the turbulent boundary layer can be shown to be approximately logarithmic [9]. Since the total stress increases linearly from the bottom surface, the total stress τ_t is expressed as:

$$\tau_t(y) = \tau_b \left(1 - \frac{y}{h}\right), \tag{4.9}$$

where y is the distance measured from the bottom of the channel. For turbulent flow moving over a solid surface, the total stress τ_t is given by Prandtl as:

$$\tau_t(y) = \rho_w l^2 \left(\frac{du}{dy}\right)^2, \tag{4.10}$$

where l is the mixing length, and $\dfrac{du}{dy}$ is the velocity gradient at a normal distance y from the bottom of the channel as done by Chow [9]. The mixing length can be defined as follow as described by Liu [11]:

$$l = Ky\sqrt{1 - \frac{y}{h}}, \tag{4.11}$$

where K is the von Karman constant. From equations (4.5), (4.9), (4.10) and (4.11) it follows that:

$$\frac{du}{dy} = \frac{\sqrt{\frac{\tau_b}{\rho_w}}}{Ky} = \frac{u_*}{Ky}. \tag{4.12}$$

Integration of equation (4.12) gives:

$$u(y) = \frac{u^*}{K} ln \left(\frac{y}{y_0}\right), \tag{4.13}$$

which is the logarithmic velocity profile distribution for the turbulent layer where y_0 is the elevation corresponding to the zero velocity level. The zero velocity level y_0 is given by Nikuradse, and is summarized in Table 4.1.

Table 4.1. Elevation corresponding to the zero velocity level for a specific flow regime.

Flow Regime:	Hydraulically smooth	Hydraulically rough	Transitional
Zero velocity level: y_0	$0.11\frac{\nu}{u_*}$	$0.033k_s$	$0.11\frac{\nu}{u_*} + 0.033k_s$

4.5 Flow resistance

Flow resistance is the influence of friction on the flow due to the channel characteristics. Factors such as surface roughness which produces a retarding effect on the flow is quantified using roughness equations and is measured in terms of a friction factor.

4.5.1 Friction factors

The most common friction factors are described by the Chezy coefficient, the Darcy-Weisbach friction factor and the Manning roughness coefficient [13]. In this study, only the Darcy-Weisbach friction factor will be considered.

For an open channel, the mean flow can be related to friction by using the Darcy-Weisbach equation as described by Francisco [14]:

$$\sqrt{\frac{8}{f}} = \frac{U}{u_*} = \frac{U}{\sqrt{gR_hS_E}}, \tag{4.14}$$

where f is the Darcy-Weisbach friction factor and S_E the energy slope of the channel. The Colebrook-White equation is used to estimate the friction factor f for turbulent open channel flows. This implicit equation, derived from experimental results of studies of turbulent flow in smooth and rough pipes, relates the friction factor f to the Reynolds

number Re and bed roughness k_s as described by Cheng [15]:

$$\frac{1}{\sqrt{f}} = -2\log\left(\frac{2.51}{Re\sqrt{f}} + \frac{k_s}{3.7D_h}\right), \tag{4.15}$$

where D_h is the hydraulic diameter, and $D_h = 4R_h$.

4.5.2 The Blasius equation

The Blasius equation is a simple equation for solving the Darcy-Weisbach friction factor. Although this equation is valid only for smooth pipes and has no term for surface roughness, it is however often used as an approximation for channels. The Blasius equation is valid for Reynolds numbers up to 10^5 and is expressed in the following way as described by Kiijarvi [16]:

$$f = \frac{0.316}{Re^{\frac{1}{4}}}, \tag{4.16}$$

where f is the Darcy-Weisbach friction factor and Re the Reynolds number.

4.5.3 Sidewall correction

In open channel flow, the hydraulic resistance of the sidewalls of the channel may not necessarily be the same as that of the bed. The sidewall friction may thus differ significantly from that of the bed. Evaluation of the bed shear stress using bulk flow parameters such as flow depth, average velocity and energy slope are often affected by the sidewall friction effects. Removing these sidewall effects is referred to as sidewall correction. Separation of the shear force exerted on the bed from that on the lateral boundaries was first proposed by Einstein [17]. The following analysis was proposed by Johnson [18], and further modified by Vanoni and Brooks [6]. The method of sidewall correction described by Vanoni and Brooks [6] for an open channel is used in this study. The method proposed, makes use of the Darcy-Weisbach formulation described in equation (4.15). This procedure consists of partitioning the cross-section of flow A into two non-interacting parts, i.e. the bed A_b and the wall A_w region, in which the streamwise component of the gravity force is resisted by the shear force exerted in the bed and walls for non-horizontal flow. Equal mean flow velocities in the bed and wall regions are assumed, and also that both partitions have the

same energy gradient. By this assumption, equation (4.14) can be expressed as:

$$\frac{U^2}{S_E} = \frac{8gA}{Pf} = \frac{8gA_b}{P_b f_b} = \frac{8gA_w}{P_w f_w}, \tag{4.17}$$

where the subscripts b and w refer to the bed and wall sections. Substituting the geometrical requirement:

$$A = A_w + A_b, \tag{4.18}$$

into equation (4.17) results in:

$$Pf = P_b f_b + P_w f_w. \tag{4.19}$$

Equation (4.19) can then be expressed as:

$$f_b = \frac{P}{P_b} f - \frac{P_w}{P_b} f_w. \tag{4.20}$$

The Reynolds numbers as described in equation (4.3) for the regions are:

$$Re = \frac{4UA}{\nu P}, \; Re_w = \frac{4UA_w}{\nu P_w} \text{ and } Re_b = \frac{4UA_b}{\nu P_b}, \tag{4.21}$$

where ν is the kinematic viscosity of water. Substituting equations (4.21) into equation (4.17) yields:

$$\frac{Re}{f} = \frac{Re_w}{f_w} = \frac{Re_b}{f_b}. \tag{4.22}$$

Since the sidewalls of the channel are smooth, Dey [3] used the Blasius equation, e.g. equation (4.16) to evaluate f_w:

$$f_w = \frac{0.316}{Re_w^{\frac{1}{4}}}. \tag{4.23}$$

By using equations (4.17) to (4.23), the following equation for the friction factor is obtained:

$$f_b = 0.036 Re_b \left(\frac{4UA}{\nu P_w} - \frac{Re_b P_b}{P_w} \right)^{-\frac{5}{4}}. \tag{4.24}$$

Substituting equations (4.21) into equation (4.15) yields:

$$\frac{1}{\sqrt{f_b}} = -2\log\left(\frac{2.51}{Re_b \sqrt{f_b}} + \frac{k_s U}{3.7 \nu Re_b} \right). \tag{4.25}$$

It is assumed that the equivalent sand roughness k_s is the same as the sand particle diameter d. For given values of $A, U, P, P_w, P_b, \nu, \rho_w$ and d, the unknowns Re_b and f_b,

e.g. the Reynolds number and friction factor associated with the bed, are determined numerically using equations (4.24) and (4.25). The bed shear stress is then calculated using equation (4.14) and knowing that $u^* = \sqrt{\frac{\tau_b}{\rho_w}}$, hence:

$$\tau_b = \frac{f_b}{8}\rho_w U^2. \tag{4.26}$$

Chapter 5

Experiments in the open-channel

The experimental part of the research was done in the Water Laboratory of the Civil Engineering Department at Stellenbosch University. All experiments were conducted in an open channel, shown in Figure 5.1. The experiments were divided into two parts. In the first part, the experiments were done on fine grained and rough grained surfaces. The objective of these sets of experiments was to determine the bed shear stress of all the sample shells. In the second part, the experiments were done on a fine grained surface, modified to co-occur with a strain gauge. The objective of these sets of experiments was to determine the drag and lift coefficients of the mussel and limpet shell samples.

Figure 5.1. The open-channel.

5.1 Experimental facilities

All experiments were conducted in an open channel. The channel had a length of 5 m, a width of 0.15 m, a depth of 0.35 m and the sidewalls were made of clear Perspex. The channel was perfectly horizontal and had a pump on the upstream end connected to a valve that controls the volume of water flowing into the channel as shown in Figure 5.1.

Water entered the open channel at the upstream end through a stilling basin to ensure a smooth water entry. The downstream end of the channel had a sluice which could be finely tuned to control the volume of water being discharged as shown in Figure 5.2.

Figure 5.2. The sluice used to manage discharge.

The water discharged from the sluice flowed into a reservoir that had a V-notch weir installed to measure the discharge, and consequently the discharge through the sluice. A barrier was placed between the upstream part of the reservoir and the downstream part of

the reservoir to minimize the ripple effect of the water such that the water level could be accurately measured at the weir as shown in Figures 5.3 and 5.4.

Figure 5.3. The barrier used to minimize the ripple effect.

Figure 5.4. The V-notch weir used to measure the discharge.

The channel bottom was elevated by constructing a ramp a distance 2 m from the upstream start point of the channel. The ramp was 2 m in length and had a height of 0.12 m, made of clear perspex. The ramp also had a removable section, which was located 1 m from the upstream end of the ramp. This section was modified to have a strain gauge attached, both in a vertical and horizontal position as seen in Figure 5.5.

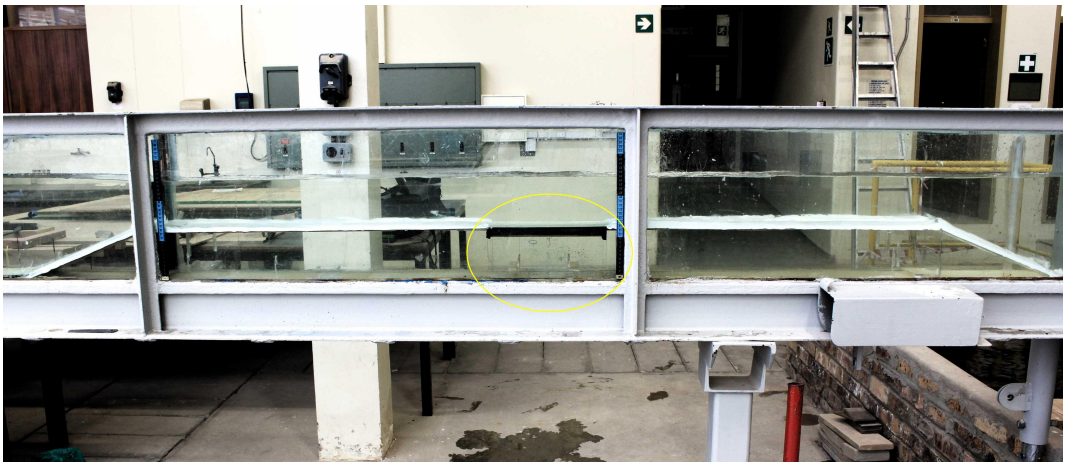

Figure 5.5. The elevated ramp with removable section.

A strain gauge is an instrument used to measure the amount of strain on an object. The

strain gauge used in these experiments consists of a metal plate which supports a metallic foil pattern. When this metallic foil deforms, it will cause changes to the electrical resistance of the foil. This change in electrical resistance is used to measure the strain on the plate. In this experiment the strain gauge was used to measure the drag and lift forces on the shells. This was done by positioning the strain gauge in the vertical position for measuring horizontal strain on the strain gauge as a result of the shell being pushed horizontally by the flow. The strain measured on the strain gauge on a horizontal position gave the vertical strain as a result of the lift force on the shell. These vertical and horizontal strains are then translated into a unit of force, in this case, Newton.

Sand particles of different sizes were glued on metal plates to simulate the different bed roughnesses, as shown in Figures 5.6 and 5.7. These plates were then submerged one by one into the channel for the different tests.

Figure 5.6. The fine grained particles on plate 1.

Figure 5.7. The rough grained particles on plate 2.

5.2 Method and results

5.2.1 Bed shear stress for incipient motion of shells

An experimental run was done for each of the sample shells on each of the plates simulating the fine and rough grained surfaces. Tests were done for each of the sample shells in an umbo upstream, convex downwards position for the mussel and limpet shells as seen in Figure 5.8 and 5.9. The same tests were done for an umbo downstream, convex upwards position for the mussel and limpet shells as seen in Figure 5.10 and 5.11. Examples of the umbo direction relative to the flow can be seen in Figure 5.12 and 5.13, which shows an umbo downstream direction for the mussel and limpet shells.

Figure 5.8. The mussel shell in a convex downwards position as seen from the frontal view.

Figure 5.9. The limpet shell in a convex downwards position as seen from the frontal view.

Figure 5.10. The mussel shell in convex upwards position as seen from the frontal view.

Figure 5.11. The limpet shell in a convex upwards position as seen from the frontal view.

These positions were chosen since a shell in any other position than these have a high probability to either slide or flip to one of these positions, thus the shell would move initially, but would immediately go to rest in one of these positions. Before starting an experimental run, the sluice at the downstream end was closed and the channel was filled with water. Each of the sample shells was then placed in the middle of the appropriate plate, making sure that no air was trapped under or around the shell. The valve at the upstream position was then gradually opened to have water enter the channel system.

Figure 5.12. The mussel shell in an umbo downstream, convex upwards position, where the arrows indicate the direction of flow.

Figure 5.13. The limpet shell in an umbo downstream, convex upwards position, where the arrows indicate the direction of flow.

Uniform flow was achieved by simultaneously opening the sluice at the downstream end, releasing the same amount water. The discharge of the sluice and the valve was then gradually adjusted to increase the velocity in the channel. This was done until the shell moved horizontally over the bed in the downstream direction. This movement was then considered as the incipient motion. When incipient motion was reached, the water level height over the V-notch weir was measured, and the discharge could then be calculated by the following equation:

$$Q = \frac{8}{15} C_d \sqrt{2g} \tan(\frac{\Theta}{2}) H^{\frac{5}{2}}, \tag{5.1}$$

where Q is the discharge, C_d the discharge coefficient for the weir, in this case $C_d = 0.58$ for the V-notch weir, g is the gravitational acceleration and has a value of 9.81 $\frac{\mathrm{m}}{\mathrm{s}^2}$, Θ is the angle of the weir, the weir used had an angle of 90 degrees, H is the water level height over the weir that was measured 0.6 m from the weir. The water level in the channel was also recorded, thus the flow area A of the channel could then be calculated using the water level height and the breadth of the channel. Since the flow area and the discharge of the channel are known, the average velocity U of the channel can be calculated using mass conservation:

$$Q_{weir} = Q_{channel} = (UA)_{channel}. \tag{5.2}$$

The bed shear stress for each of the plates and shells are then calculated by following the method explained in Section 4.5.3. The values of the bed shear stress, average flow velocity and bed roughness for the sample shells for each of the different bed plates and positions are given in Table 5.1 and Table 5.2, where d is the bed roughness.

Table 5.1. The values of average flow velocity, flow height and bed shear stress for shells in a umbo downstream, convex upwards position.

	Fine grained surface d=0.3mm			Rough grained surface d=0.9mm		
Sample	h (m)	U (m/s)	τ_b (Pa)	h (m)	U (m/s)	τ_b (Pa)
Mussel 1	0.1635	0.8151	2.1485	0.1535	0.8826	3.2764
Mussel 2	0.1885	0.7789	1.9528	0.1635	0.8018	2.7011
Mussel 3	0.1555	0.7750	1.9542	0.1435	0.9753	4.0073
Mussel 4	0.1385	0.8406	2.3033	0.1585	1.0168	4.3177
Mussel 5	0.1535	0.8260	2.2125	0.1735	1.0616	4.6709
Mussel 6	0.1795	0.6045	1.2013	0.1935	0.8202	2.7936
Mussel 7	0.1535	0.8260	2.2125	0.1885	0.9631	3.8358
Mussel 8	0.1555	0.7230	1.7090	0.1835	0.8128	2.7534
Mussel 9	0.1535	0.7454	1.8140	0.1635	0.8980	3.3743
Mussel 10	0.1585	0.7866	2.0091	0.1585	0.9117	3.4842
Mussel 11	0.1785	0.6298	1.3003	0.1635	0.8980	3.3743
Mussel 12	0.1635	0.7755	1.9512	0.1635	0.8980	3.3743
Mussel 13	0.1235	0.8323	2.2769	0.1585	0.9117	3.4842
Mussel 14	0.1375	1.0678	3.6655	0.1635	1.1103	5.1231
Mussel 15	0.1635	0.8151	2.1485	0.1685	1.0310	4.4184
Mussel 16	0.1635	0.8018	2.0810	0.1735	0.9719	3.9265
Mussel 17	0.1535	0.9117	2.6785	0.1435	0.9753	4.0073
Mussel 18	0.1705	0.6594	1.4237	0.1635	0.9267	3.5895
Mussel 19	0.1685	0.6909	1.5589	0.1685	0.9275	3.5886
Mussel 20	0.1465	0.8655	2.4286	0.1635	1.0625	4.6981
Mussel 21	0.1515	0.8091	2.1274	0.1635	1.0008	4.1758
Mussel 22	0.1735	0.6827	1.5210	0.1735	0.9574	3.8122
Mussel 23	0.1885	0.6393	1.3345	0.1685	0.9419	3.6988
Mussel 24	0.1535	0.8260	2.2125	0.1535	1.0986	5.0398
Mussel 25	0.1585	0.9559	2.9305	0.1685	1.0310	4.4184
Mussel 26	0.1535	0.7986	2.0725	0.1585	0.9263	3.5946
Mussel 27	0.1915	0.6733	1.4732	0.1635	0.8286	2.8813
Mussel 28	0.1635	0.6876	1.5470	0.1935	0.8715	3.1467
Mussel 29	0.1785	0.6985	1.5869	0.1435	0.9753	4.0073
Mussel 30	0.1685	0.7275	1.7218	0.1635	0.7886	2.6144
Mussel 31	0.1535	0.8400	2.2853	0.1435	0.8985	3.4107
Mussel 32	0.1635	0.8560	2.3616	0.1485	0.9424	3.7365
Limpet 1	0.1385	0.7421	1.8103	0.1585	0.7866	2.6073
Limpet 2	0.1535	0.8826	2.5152	0.1685	0.8306	2.8886
Limpet 3	0.1385	0.7834	2.0100	0.1685	0.7652	2.4592
Limpet 4	0.1435	0.7294	1.7470	0.1655	0.7035	2.0878
Limpet 5	0.1425	0.7889	2.0336	0.1565	0.7569	2.4197

Table 5.2. The values of average flow velocity, flow height and bed shear stress for shells in a umbo upstream, convex downwards position.

	Fine grained surface d=0.3mm			Rough grained surface d=0.9mm		
Sample	h (m)	U (m/s)	τ_b (Pa)	h (m)	U (m/s)	τ_b (Pa)
Mussel 27	0.1255	0.1816	0.1266	0.1745	0.1139	0.0620
Mussel 28	0.1335	0.2006	0.1516	0.1935	0.1178	0.0657
Mussel 29	0.1335	0.1883	0.1348	0.1515	0.1997	0.1822
Mussel 30	0.1485	0.1804	0.1236	0.1885	0.1421	0.0938
Mussel 31	0.1635	0.2199	0.1777	0.1555	0.1466	0.1007
Mussel 32	0.1665	0.2159	0.1716	0.1585	0.1438	0.0970
Limpet 1	0.1935	0.1384	0.0748	0.1885	0.1169	0.0649
Limpet 2	0.1735	0.1449	0.0819	0.1985	0.1570	0.1131
Limpet 3	0.1685	0.1492	0.0865	0.1985	0.1570	0.1131
Limpet 4	0.1935	0.1518	0.0886	0.1735	0.1449	0.0979
Limpet 5	0.1735	0.1544	0.0920	0.1635	0.1173	0.0659

For the fossilized shells, the same methodology was used as for the mussel and limpet samples. Since the fossilized shells where covered in phosphate, experimental tests were firstly done on the shells in their dirty states. The shells were then cleaned and the tests were done again to record the difference between the shells in their dirty and clean states. The values of the bed shear stress, average flow velocity and bed roughness for the dirty and clean sample shells are given in Table 5.3 and 5.4, respectively.

Table 5.3. The fossilized shells in their dirty states.

	Fine grained surface d=0.3mm			Rough grained surface d=0.9mm		
Sample	h (m)	U (m/s)	τ_b (Pa)	h (m)	U (m/s)	τ_b (Pa)
Clam 1	0.1735	3.8303	44.2331	0.1635	3.4741	48.7980
Clam 2	0.1635	2.9086	25.7999	0.1645	2.8909	33.8958
Clam 3	0.1735	3.7981	43.5007	0.1635	3.1404	39.9512
Clam 4	0.1635	4.6491	65.0700	0.1755	4.4385	78.8932
Clam 5	0.1635	3.6875	41.1827	0.1635	3.0596	37.9427
Twirl 1	0.1935	0.2017	0.1500	0.1585	0.3178	0.4448
Twirl 2	0.1685	0.2918	0.3014	0.1535	0.2898	0.3728
Twirl 3	0.1785	0.3480	0.4191	0.1635	0.2452	0.2687
Cone 1	0.1735	1.2038	4.5652	0.1585	1.0799	4.8613
Cone 2	0.1885	0.5354	0.9494	0.1535	0.6336	1.7097
Cone 3	0.1735	0.7937	2.0338	0.1635	0.7245	2.2139
Cylinder 1	0.1885	0.3009	0.3176	0.1785	0.2822	0.3507
Cylinder 2	0.1635	0.2584	0.2403	0.1735	0.3120	0.4264
Cylinder 3	0.1785	0.1746	0.1153	0.1935	0.2418	0.2590

Table 5.4. The fossilized shells in their clean states.

	Fine grained surface d=0.3mm			Rough grained surface d=0.9mm		
Sample	h (m)	U (m/s)	τ_b (Pa)	h (m)	U (m/s)	τ_b (Pa)
Clam 1	0.1485	0.7438	1.8102	0.1255	1.0620	3.6493
Clam 2	0.1435	0.7561	1.8726	0.1615	0.7984	2.0652
Clam 3	0.1385	0.7834	2.0100	0.1435	2.1844	2.8123
Clam 4	0.1385	0.9155	2.7174	0.1385	1.0939	3.8403
Clam 5	0.1735	0.5605	1.0410	0.1635	0.6876	1.5470
Twirl 1	0.1835	0.2550	0.2330	0.1435	0.2868	0.2945
Twirl 2	0.1435	0.2046	0.1566	0.1785	0.3032	0.3231
Twirl 3	0.2035	0.1670	0.1055	0.2035	0.2076	0.1580
Cone 1	0.1635	0.8749	2.4637	0.1735	1.0897	3.7607
Cone 2	0.1685	0.4931	0.8158	0.1785	0.5806	1.1119
Cone 3	0.1705	0.7286	1.7256	0.1735	0.5628	1.0493
Cylinder 1	0.1735	0.4079	0.5673	0.1585	0.4560	0.7050
Cylinder 2	0.1785	0.2961	0.3090	0.1735	0.3660	0.4619
Cylinder 3	0.1935	0.1472	0.0838	0.2035	0.2076	0.1580
Fragment 1	0.1385	0.7558	1.8750	0.1215	0.6461	1.3983
Fragment 2	0.1445	0.7244	1.7230	0.1235	0.6357	1.3535
Fragment 3	0.1185	0.5359	0.9781	0.1735	0.3993	0.5448
Fragment 4	0.1435	0.7294	1.7470	0.1535	0.5761	1.1048
Fragment 5	0.1335	0.8873	2.5638	0.1235	0.9103	2.7087
Fragment 6	0.1335	0.5762	1.1146	0.1935	0.5810	1.1091

5.2.2 Lift and drag forces of shells

The drag forces on the shells were measured for the mussel and limpet shells. This was done with the use of a strain gauge for the shells in a convex upward position. A non stretchable and lightweight cord was used to attach the shell to the strain gauge. Various positions of the shell were considered to find the stable position of the shell, i.e. the position of least drag. An example of an attachment of the shell to the strain gauge is seen in Figure 5.14.

Figure 5.14. An example of the mussel shell for the convex upward position attached to the strain gauge to measure the drag force.

It was found that the position of least drag was in the umbo downstream position as considered in Section 5.2.1. The shell was then placed like a dome over the strain gauge making sure no air was trapped inside in such a way that the connecting cord was slack and not pulling on the strain gauge. The flow velocity in the channel was then increased incrementally until incipient motion was reached with the cord tight. The drag force was

recorded for the whole experimental run as illustrated in Figure 5.15

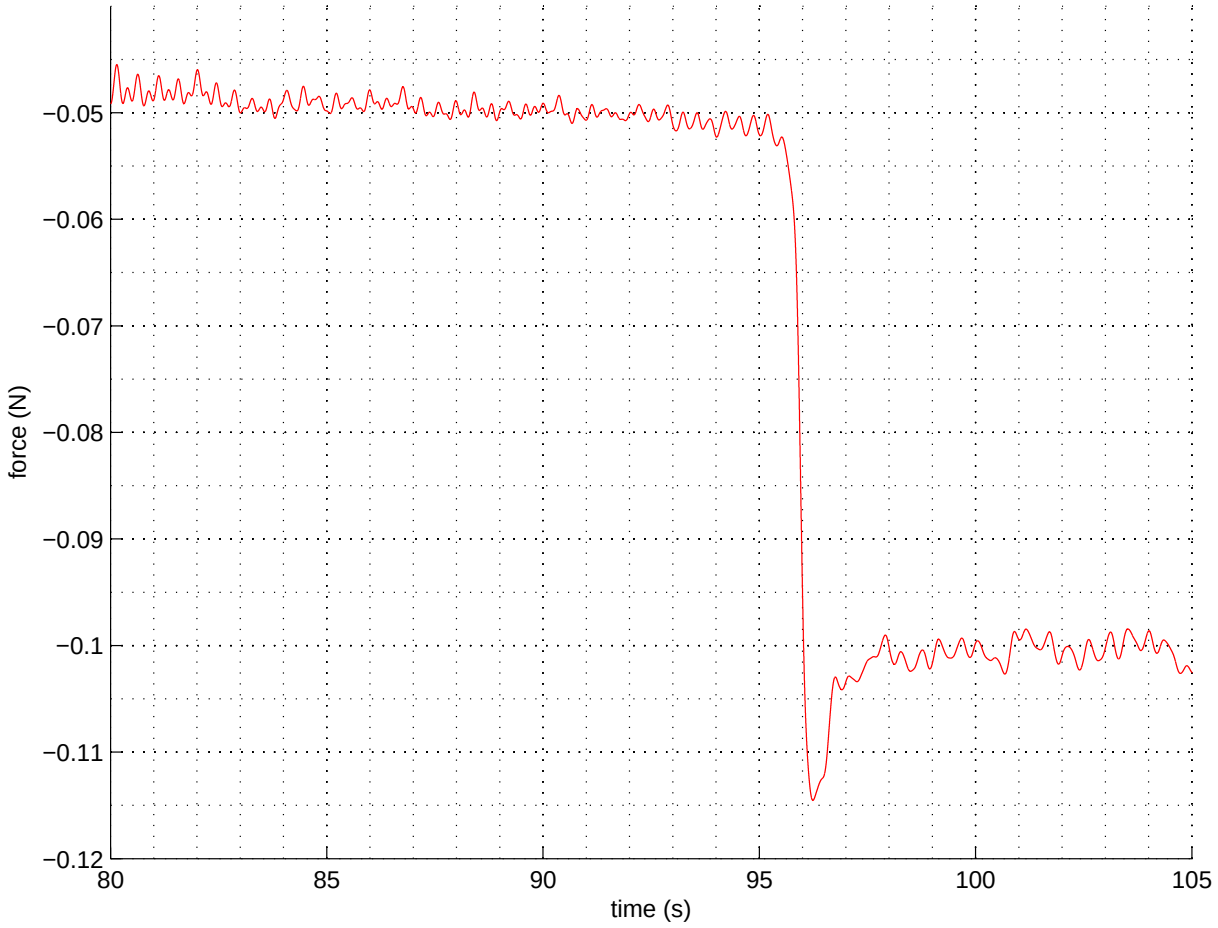

Figure 5.15. Graph of an experimental run showing drag force measured on the shell versus time with incipient motion reached at 96 seconds.

The graph in Figure 5.15 shows a force of approximately 0.05 N on the strain gauge before it reaches incipient motion. The negative values of the force are only an indication of the direction the force was measured relative to the strain gauge, thus the absolute value is taken. The shell reached incipient motion at approximately 95 seconds. After incipient motion was reached, the strain gauge measured a force of approximately 0.1 N. The spike in the graph seen at 96 seconds is a result from the momentum of the shell when the cord is pulled tight, and is thus ignored. The drag force on the shell is calculated by taking the difference of the drag force measurement on the strain gauge before and after incipient motion is reached, i.e. $0.1\,\mathrm{N} - 0.05\,\mathrm{N}$. A drag force of approximately 0.05 N is thus mea-

sured for the experimental run shown in the graph of Figure 5.15. The experimental run was repeated 5 times, recording an average drag force of 0.0427 N. The same experimental runs were done for the limpet shell. It was found that the position of least drag was also in the umbo downstream position. The drag force versus the time of an experimental run is shown in Figure 5.16.

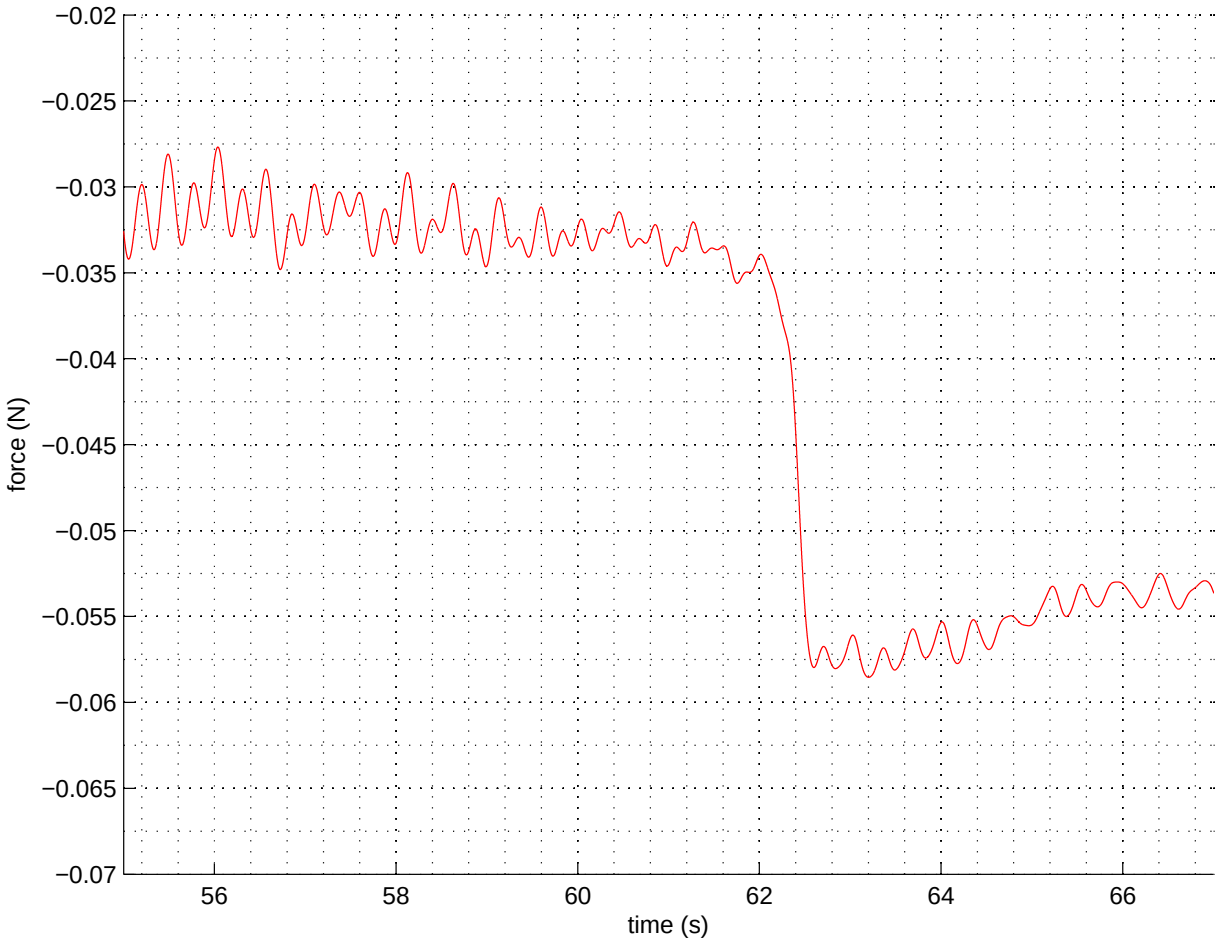

Figure 5.16. Graph of experimental run showing drag force measured on the shell versus time with incipient motion reached at 62 seconds.

The graph in Figure 5.16 shows the limpet shell reaching incipient motion at about 62 seconds. The force measured on the strain gauge before incipient motion was reached, is approximately 0.033 N. The force measured on the strain gauge after incipient motion was reached is approximately 0.056 N. The difference between the force before and after incipient motion is approximately 0.023 N, i.e. 0.056 N − 0.033 N, for the experimental run

shown. This experimental run was repeated 3 times, recording an average drag force of 0.0233 N.

The lift forces of the mussel and limpet shells were measured next. This was done with the use of the strain gauge in the horizontal position for the shells in a convex upward position as done previously. The shells for these tests were attached onto the strain gauge using a toothpick that was attached vertically to the strain gauge in the horizontal position. The shells were then glued onto the top point of the toothpick such that the shell would lay lightly on the surface of the channel as seen in Figure 5.17. The channel was then filled with water while all valves were closed such that there was no flow velocity in the channel. The trapped air under the shell was then removed with an needle through a small hole that was drilled into the top of the shell. This is seen in Figure 5.18.

Figure 5.17. Attaching the shell to the strain gauge

Figure 5.18. Removing trapped air under shell with the use of a needle.

After all the air was removed, the flow velocity was gradually increased over a period of time with all force data recorded. When the flow conditions in the channel met the condition under which incipient motion should be reached, the time at that instant was recorded. The force measured at that instant was then used as the lift force caused by the flow. An experimental run for the mussel shell can be seen in Figure 5.19 and an experimental run for the limpet shell is seen in Figure 5.20.

Figure 5.19 shows a force of approximately 0.065 N on the strain gauge when there is a zero velocity of flow in the channel.

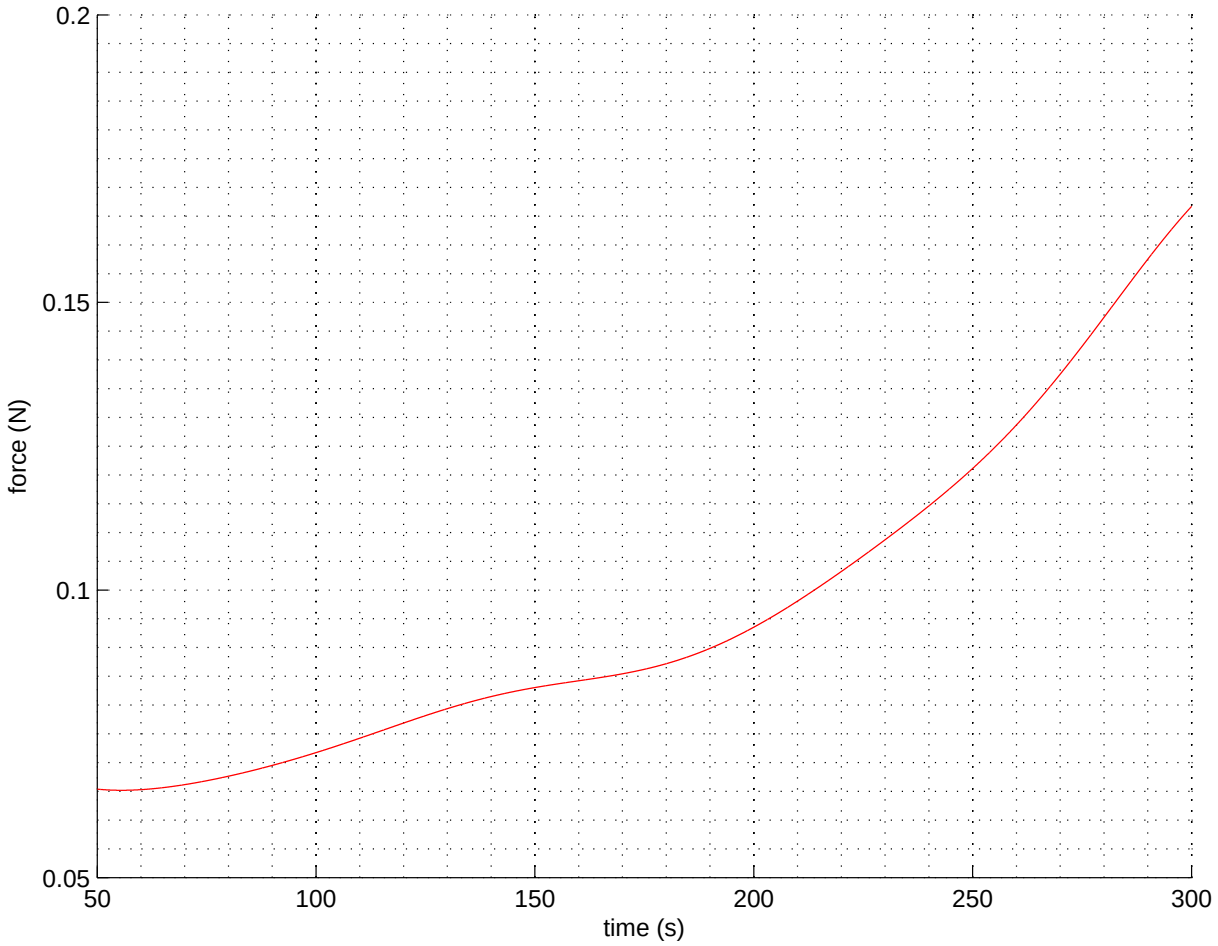

Figure 5.19. Graph of experimental run showing lift force measured on mussel shell versus time.

This force results from the weight of the shell and toothpick. The flow velocity in the channel is then gradually increased until the flow conditions for incipient motion are met, at 300 seconds in this case. The strain gauge at 300 seconds measures a force of approximately 0.165 N. To calculate the lift force on the shell, the difference of the force measured when there is a zero velocity in the channel and the force measured when the conditions for incipient motion is reached in the channel must be taken, i.e. $0.165\,\mathrm{N} - 0.065\,\mathrm{N}$, which gives a force of approximately 0.1 N. The same process can be seen in Figure 5.20 for the limpet

shell. Figure 5.20 shows a force of approximately 0.045 N when there is a zero velocity of flow in the channel for the limpet shell. The incipient conditions for the limpet shell are met at approximately 290 seconds, giving a force of approximately 0.073 N. The lift force due to only the flow velocity on the limpet shell would then be approximately 0.028 N. These experimental runs were done three times, both for the mussel and the limpet shell. The average lift force for the mussel was calculated to be 0.1 N and the average lift force for the limpet was calculated to be 0.028 N.

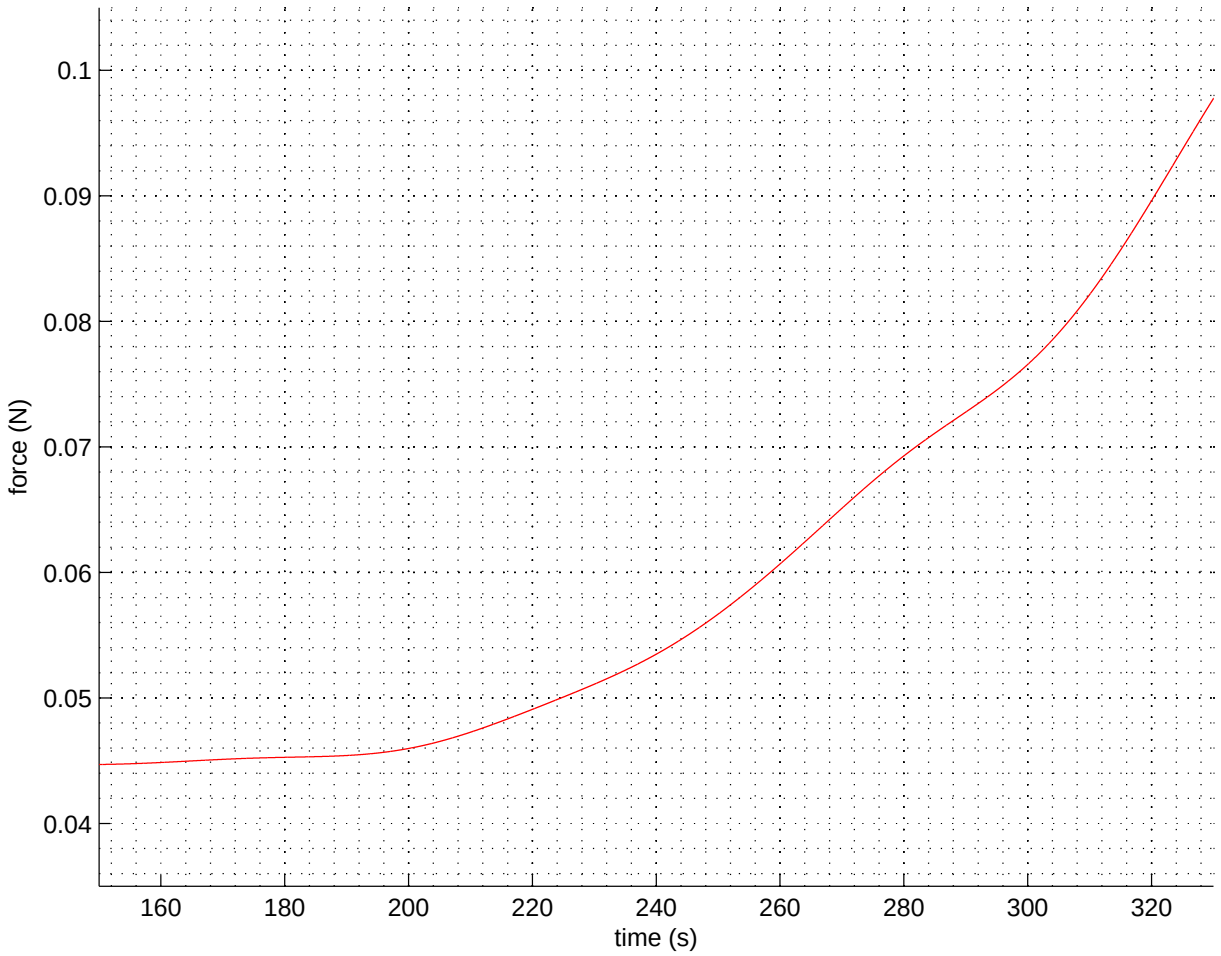

Figure 5.20. Graph of experimental run showing lift force measured on limpet shell versus time.

Chapter 6

Forces on a single shell

The forces on a shell where the flow is in a specific direction and approximately parallel, with low turbulent streamlines are the forces due to gravitation, drag, lift and friction. The force due to gravitation F_G is the downwards force as a result of its submerged weight. The drag force F_D and the lift force F_L are a consequence of the hydrodynamic forces caused by the flow of the water. The force due to friction is known as the static coulomb friction force F_S between the shell and the bed [3]. These forces are illustrated in Figure 6.1.

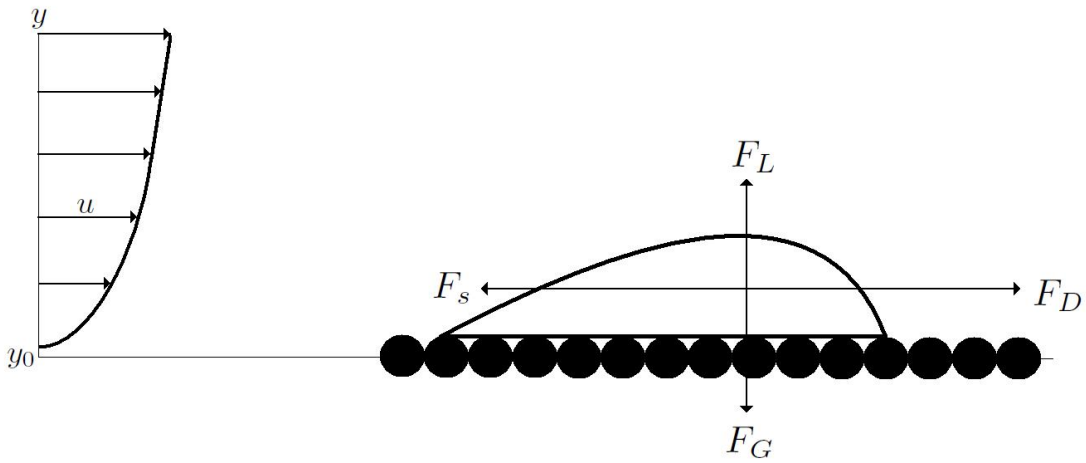

Figure 6.1. Forces on a single shell

6.1 Forces at the critical stage

At the critical stage where the shell starts to move relative to the bed, the drag force will be equal to the friction force, i.e. $F_D = F_S$. The critical friction force can be expressed as:

$$F_s = \mu_c N, \tag{6.1}$$

where μ_c is the static Coulomb friction factor and N is the normal force. From Figure 6.1, it follows that the normal force is:

$$N = F_G - F_L. \tag{6.2}$$

From equation (6.1) and (6.2) it follows that:

$$F_S = (F_G - F_L)\mu_c. \tag{6.3}$$

Figure 6.2 shows the critical friction force F_S between an inclined plane and a shell. The angle of friction ϕ is measured by gradually increasing the inclination angle of the plane until the shell is just about to slide down the plane.

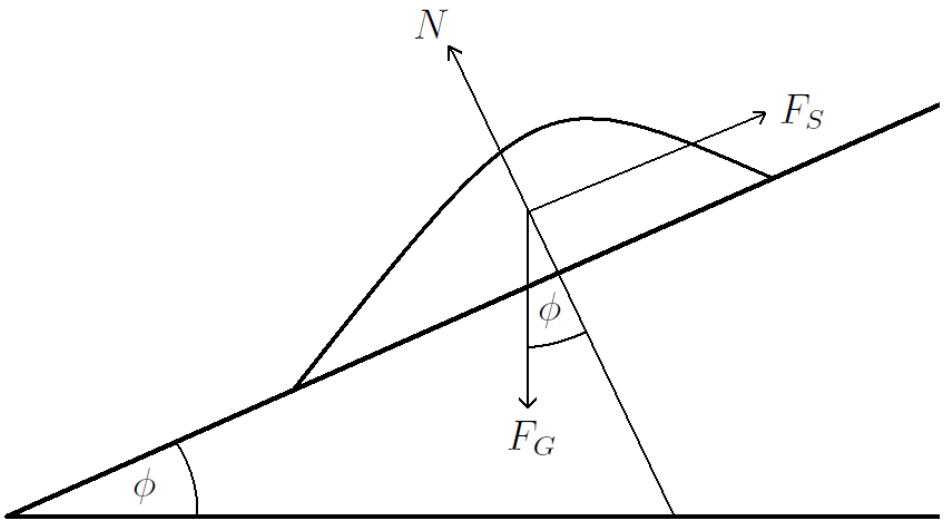

Figure 6.2. The shell lying on an inclined plane.

When the shell is just about to slide down the plane, the forces in Figure 6.2 can be

expressed as:

$$F_s = F_G \sin\phi \tag{6.4}$$

and

$$N = F_G \cos\phi. \tag{6.5}$$

From equations (6.1), (6.4) and (6.5), the static Coulomb friction factor is expressed as:

$$\mu_c = \tan\phi. \tag{6.6}$$

This provides a reasonable approximation of the angle of friction ϕ between the shell and the bed [3]. For the critical stage where $F_S = F_D$ and substituting equation (6.6) into equation (6.3) yields:

$$F_D = (F_G - F_L)\tan\phi. \tag{6.7}$$

The submerged weight of the shell is expressed as:

$$F_G = V(\rho_s - \rho_w)g, \tag{6.8}$$

where V is the volume of the shell and ρ_s is the mass density of the shell. The drag force F_D is expressed as:

$$F_D = 0.5 C_D \rho_w U_m^2 A_p, \tag{6.9}$$

where C_D is the drag coefficient, U_m the mean flow velocity received by the frontal area A_p of the shell. The lift force F_L caused by the shear flow is expressed as:

$$F_L = 0.5 C_L \rho_w U_m^2 A_s, \tag{6.10}$$

where C_L is the lift coefficient. Solving equations (6.9) and (6.10) requires the unknowns A_p, C_D, C_L and U_m to be determined. The methods to solve these variables are described in the following subsections.

6.2 Determination of the frontal area A_p

The frontal area is the area of the shell which is exposed to the flow when the shell is in the position of least drag. The frontal area of the mussel, limpet, clam shells and fossilized shell fragments are approximated by a segment of a circular arc having a height c and a

chord length l_c. The area is given by:

$$A_p = 0.25c^2 \left(0.25 \left(\frac{l_c}{c}^2\right) + 1\right)^2 \xi, \tag{6.11}$$

where

$$\xi = \arccos\left(\frac{\left(\frac{l_c}{c}\right)^2 - 4}{\left(\frac{l_c}{c}\right)^2 + 4}\right) - 4\left(\frac{l_c}{c}\right)\left(\frac{\left(\frac{l_c}{c}\right)^2 - 4}{\left(\left(\frac{l_c}{c}\right)^2 + 4\right)^2}\right). \tag{6.12}$$

The frontal area of the cone shape shell is determined by that of a circle, thus:

$$A_p = \pi\left(\frac{b}{2}\right)^2, \tag{6.13}$$

where b is the breadth of the shell which is the same as the diameter of the shell. The frontal area of the cylinder shaped shell is approximated by that of a rectangle, thus:

$$A_p = ac, \tag{6.14}$$

where a is the length and c is the height of the cylinder. The frontal area of the twirl shaped shell is approximated by that of a parallelogram:

$$A_p = a_b c, \tag{6.15}$$

where a_b is the length of the base and c the height of the parallelogram.

6.3 Determination of mean velocity U_m

Solving equations (6.9) and (6.10) to determine the drag C_D and lift C_L requires values for the mean velocity of the shells. The mean velocity of the flow received by the frontal area of the shell is given by:

$$U_m = \frac{1}{A_p}\int_{\frac{k_s}{2}}^{\frac{k_s}{2}+c} xu\mathrm{d}y. \tag{6.16}$$

Solving equation (6.16) requires a function x to be integrated over the y-axis, between the boundaries $\frac{k_s}{2}$ and $\frac{k_s}{2} + c$. The function x is determined by the frontal shape of the shell. For the mussel, limpet, fossilized clam and shell fragments, the frontal shape of the shell

is described by that of a circular arc as seen in Figure 6.3.

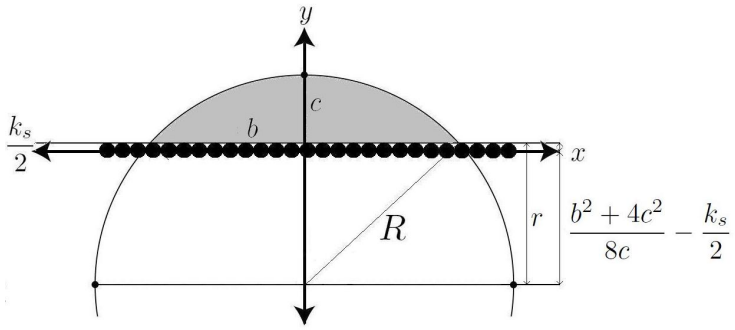

Figure 6.3. The frontal shape approximated by a circular arc.

From Figure 6.3 it can be seen that:

$$r = R - c. \tag{6.17}$$

By squaring both sides of equation (6.17), the following equation is derived:

$$r^2 = R^2 - 2Rc + c^2, \tag{6.18}$$

which is then written as:

$$R^2 - r^2 = 2Rc - c^2. \tag{6.19}$$

By using the Pythagorean theorem, the length b is expressed as:

$$b = 2\sqrt{R^2 - r^2}. \tag{6.20}$$

Substituting equation (6.19) into equation (6.20), the following expression is derived:

$$b = 2\sqrt{c(2R - c)}. \tag{6.21}$$

From equation (6.21), the radius R of the circle in Figure 6.3 is expressed in terms of the shells breadth b and height c:

$$R = \frac{b^2 + 4c^2}{8c}. \tag{6.22}$$

Substituting equation (6.17) into equation (6.22), the length r can be expressed as:

$$r = \sqrt{R^2 - \frac{b^2}{4}}. \tag{6.23}$$

By substituting $R = r + c$ into equation (6.22), r can be expressed as:

$$r = \frac{b^2 - 4c^2}{8c}. \tag{6.24}$$

The equation of a circle is given by:

$$x^2 + y^2 = R^2 \tag{6.25}$$

The x-axis is then moved downwards by a distance of $\frac{k_s}{2}$ as seen in Figure 6.3, this is done to simulate how the shell would rest on the sand grains since the shell does not rest on the bed described by the x-axis. Substituting equation (6.22) and equation (6.23) into equation (6.25), the equation of the circle becomes:

$$x^2 + (y + \frac{b^2 - 4c^2}{8c} - \frac{k_s}{2})^2 = (\frac{b^2 + 4c^2}{8c})^2. \tag{6.26}$$

Solving x for the positive root only, it follows that:

$$x = \sqrt{(\frac{b^2 + 4c^2}{8c})^2 - (y + \frac{b^2 - 4c^2}{8c} - \frac{k_s}{2})^2}. \tag{6.27}$$

For the shell in a convex downward position, equation (6.27) would be written as:

$$x = \sqrt{(\frac{b^2 + 4c^2}{8c})^2 - (y - \frac{b^2 - 4c^2}{8c} - \frac{k_s}{2})^2}. \tag{6.28}$$

For the cone shell, the frontal shape exposed to the flow is determined by that of a circle. The same method as for the circle is used, where the segment of a circular arch is now replaced by that of a circle. The positive side of the circle is described by the following equation:

$$x = \sqrt{(\frac{b}{2})^2 - (y - \frac{k_s}{2} - \frac{b}{2})^2}. \tag{6.29}$$

For the shell shaped as a cylinder, the frontal shape exposed to the flow is approximated by that of a rectangle since the shell rolls along its side like a barrel. A equation of a straight horizontal line describes the shell:

$$x = a. \tag{6.30}$$

For the shell shaped as a twirl, the frontal shape exposed to the flow is approximated by that of a parallelogram, where $\frac{1}{S_G}$ is the gradient of the side of the shell when lying flat on

the ground. The frontal shape of the shell is then described by the following equation:

$$x = \frac{y}{S_G} - \frac{y - y_{int}}{S_G}, \tag{6.31}$$

where y_{int} is the y axis intercept of the line described by the gradient $\frac{1}{S_G}$ and the appropriate side length of the shell.

The velocity distribution u is approximated by the following function as described in Section 4.4.4 for flow in the turbulent layer:

$$u = \frac{u_*}{K}\ln(\frac{y}{y_0}), \tag{6.32}$$

where u_* is the shear velocity, it is expressed as $u_* = \sqrt{\frac{\tau_b}{\rho_w}}$. K is known as the von Karman constant and $K = 0.41$ [3]. y_0 is the zero velocity level above the virtual bed, as described in Section 4.4.4, the virtual bed in this case is the x-axis. The zero velocity level height has been experimentally shown to be a factor of 0.033 of the sand particle diameter, thus $y_0 = 0.033k_s$, as listed in Table 4.1. To determine the mean velocities for the mussel and limpet shells, equations (6.27) and (6.32) are substituted into equation (6.16), yielding:

$$U_m = \frac{2}{A_p}\int_{\frac{k_s}{2}}^{\frac{k_s}{2}+c} \sqrt{(\frac{b^2+4c^2}{8c})^2 - (y + \frac{b^2-4c^2}{8c} - \frac{k_s}{2})^2} \times \frac{u_*}{K}\ln(\frac{y}{y_0})\mathrm{dy}, \tag{6.33}$$

which is then written as:

$$U_m = \frac{2}{A_p K}\sqrt{\frac{\tau_b}{\rho}}\int_{\frac{k_s}{2}}^{\frac{k_s}{2}+c} \sqrt{(\frac{b^2+4c^2}{8c})^2 - (y + \frac{b^2-4c^2}{8c} - \frac{k_s}{2})^2} \times \ln(\frac{y}{y_0})\mathrm{dy}. \tag{6.34}$$

The mean velocities U_m for each of the sample shells in the convex upward position for the fine and the rough grained surface using equation (6.34) is summarized in Table 6.1. The values for the bed shear stress τ_b recorded by the experimental runs were used to solve equation (6.34).

Table 6.1. Mean velocities for the shells in a convex upward position by using equation (6.34)

Sample	U_m fine	U_m rough	Sample	U_m fine	U_m rough
Mussel 1	0.674	0.694	Mussel 20	0.656	0.756
Mussel 2	0.633	0.621	Mussel 21	0.622	0.722
Mussel 3	0.634	0.756	Mussel 22	0.532	0.699
Mussel 4	0.683	0.778	Mussel 23	0.487	0.671
Mussel 5	0.669	0.809	Mussel 24	0.627	0.784
Mussel 6	0.497	0.631	Mussel 25	0.721	0.734
Mussel 7	0.674	0.740	Mussel 26	0.717	0.794
Mussel 8	0.579	0.611	Mussel 27	0.523	0.607
Mussel 9	0.596	0.677	Mussel 28	0.536	0.635
Mussel 10	0.633	0.694	Mussel 29	0.579	0.768
Mussel 11	0.505	0.677	Mussel 30	0.586	0.601
Mussel 12	0.619	0.677	Mussel 31	0.685	0.698
Mussel 13	0.662	0.681	Mussel 32	0.685	0.717
Mussel 14	0.848	0.833	Limpet 1	0.674	0.681
Mussel 15	0.643	0.766	Limpet 2	0.717	0.640
Mussel 16	0.640	0.731	Limpet 3	0.659	0.609
Mussel 17	0.719	0.731	Limpet 4	0.579	0.526
Mussel 18	0.514	0.677	Limpet 5	0.576	0.520
Mussel 19	0.538	0.678			

6.4 Determination of the drag coefficient C_D and the lift coefficient C_L

From forces on a single shell in Section 6.1, it is known that the drag force is expressed as:

$$F_D = 0.5 C_D \rho_w U_m^2 A_p, \tag{6.35}$$

and the lift force by:

$$F_L = 0.5 C_L \rho_w U_m^2 A_s. \tag{6.36}$$

Experimental tests were done on the limpet and mussel shell to determine the drag and lift forces as described in Section 5.2.2. These tests were done on the Mussel 26 and the Limpet 1 shell samples. By using equations (6.35) and (6.36), and the lift and drag force values obtained from the experiment, the drag and lift coefficients were calculated for

those specific samples. All values for variables needed as well is the calculated drag and lift coefficients are summarized in Table 6.2. Equation 6.11 is used to calculate the the frontal area A_p for both shells.

Table 6.2. Drag and lift Coefficients for shells in the convex upward position

Sample	U_m	A_p	A_s	F_D	F_L	C_D	C_L
Mussel 26	0.717	0.000794	0.004921	0.0427	0.1	0.210	0.079
Limpet 1	0.674	0.000982	0.002989	0.0233	0.028	0.105	0.041

Due to the nature of the shape and size of the fossilized shells, strain gauge experiments could not be implemented to determine the drag and lift forces. Since the shape of the fossilized clam and shell fragments closely relates to that of the limpet shell, it is assumed to have the same drag and lift properties. For the cone, twirl and cylinder shaped shells, fall velocity tests were done in a test tube to determine the drag coefficients. The fall velocity tests in the test tube only gives relevant results if the shells fall in the same orientation through the water in the test tube under gravity than what it moved on the bed at incipient motion. This was the case for the cone, twirl and cylinder shaped shells. Measuring the time it takes the shell to fall a distance in the test tube, the mean velocity U_m can be calculated for each of those sample shells. The drag coefficients C_D is then calculated for each of these shells using equation (6.35). For the cone shaped shell, even under very high velocities, no visible lift force was observed. It is thus assumed that the cone shaped shell had no lift coefficient. The twirl and cylinder shaped shells are assumed to have a lift coefficient the same as that of a cylinder in cross flow [19]. The Drag and lift coefficients for all the shells are summarized in Table 6.3

Table 6.3. Drag and lift Coefficients for shells

Shell	C_D	C_L
Cone	0.34	0
Twirl	1.22	0.07
Cylinder	1.22	0.07
Clamp	0.105	0.041
Fragment	0.105	0.041

Chapter 7

The bed shear stress τ_b of the shells

In this chapter a general analytical equation is derived for solving the bed shear stress of a shell. This is done by using the equations of forces on a single shell at the critical stage of incipient motion as described in Section 6.1. An analytical equation for solving the bed shear stress of each type of shell is then derived. This analytical equation is then used to determine the bed shear stresses for each of the sample shells by only using the characteristic properties of them. The analytical results of the bed shear stresses are then compared to the results determined by the experiments.

7.1 General analytical equation for the bed shear stress τ_b of a shell

It is known from forces on a single shell that the drag force F_D can be written in terms of the force F_G resulting from gravitation, the lift force F_L and the angle of friction ϕ as expressed by equation (6.7). The force due to gravity is expressed by equation (6.8), the drag and lift forces are described by equations (6.9) and (6.10), respectively.

By substituting equations (6.16), (6.8), (6.9) and (6.10) into equation (6.7), a general expression for the bed shear stress is obtained for a shell:

$$\tau_b = \frac{\rho_w V(\rho_s - \rho_w) g \tan\phi}{[\frac{1}{A_p K}\int_{\frac{k_s}{2}}^{\frac{k_s}{2}+c} xu\mathrm{d}y]^2(0.5C_D\rho_w A_p + 0.5C_L\rho_w A_s \tan\phi)}. \tag{7.1}$$

The variable x in equation (7.1) is the function that describes the frontal area of a specific shell as described in Section 6.3. The variable u is the logarithmic velocity profile distribution as described in Section 4.4.4. The logarithmic velocity profile distribution, e.g. equation (4.13), as well as the shear velocity $u_* = \sqrt{\frac{\tau_b}{\rho_w}}$ is substituted into equation (7.1).

7.2 Analytical equation of the bed shear stress τ_b for each shell

An expression for the bed shear stress of each of the different shells are obtained from equation (7.1). This is done by substituting the function x describing the shape of the frontal area of each shell into the general equation of bed shear stress for a shell, e.g. equation (7.1). The frontal shape of the mussel, limpet, fossilized clam and shell fragments are described by the function in equation (6.27), for the shells in a convex upward position. Since the function x only describes the positive root, e.g. half of the frontal area of the shell, the value of the integral is multiplied by a factor of 2. Substituting equation (6.27) into equation (7.1) results in the following expression for the bed shear stress of the mussel, limpet, fossilized clam and shell fragments:

$$\tau_b = \frac{\rho_w V(\rho_s - \rho_w) g \tan\phi}{[\frac{2}{A_p K}\int_{\frac{k_s}{2}}^{\frac{k_s}{2}+c} \sqrt{(\frac{b^2+4c^2}{8c})^2 - (y + \frac{b^2-4c^2}{8c} - \frac{k_s}{2})^2} \times \ln(\frac{y}{y_0})\mathrm{d}y]^2 (0.5 C_D \rho_w A_p + 0.5 C_L \rho_w A_s \tan\phi)}. \tag{7.2}$$

The same methodology is followed for the rest of the shells. The frontal shape of the cone shell is described by the function expressed in equation (6.29). Substituting equation (6.29) into equation (7.1) results in the following expression for the bed shear stress of the Cone shell:

$$\tau_b = \frac{\rho_w V(\rho_s - \rho_w) g \tan\phi}{[\frac{2}{A_p K}\int_{\frac{k_s}{2}}^{\frac{k_s}{2}+b} \frac{2}{A_p K}\sqrt{(\frac{b}{2})^2 - (y - \frac{k_s}{2} - \frac{b}{2})^2} \times \ln(\frac{y}{y_0})\mathrm{d}y]^2 (0.5 C_D \rho_w A_p + 0.5 C_L \rho_w A_s \tan\phi)}. \tag{7.3}$$

The frontal shape of the cylinder shaped shell is described by the function in equation (6.30). Substituting equation (6.30) into equation (7.1) results in the following ex-

pression for the bed shear stress of the cylinder shaped shell:

$$\tau_b = \frac{\rho_w V(\rho_s - \rho_w)\text{gtan}\phi}{[\frac{1}{A_p K}\int_{\frac{k_s}{2}}^{\frac{k_s}{2}+b} a \times \ln(\frac{y}{y_0})\text{dy}]^2(0.5C_D\rho_w A_p + 0.5C_L\rho_w A_s\text{tan}\phi)}. \tag{7.4}$$

The frontal shape of the twirl shaped shell is described by the function in equation (6.31). Substituting equation (6.31) into equation (7.1), results in the following expression for the bed shear stress of the twirl shaped shell:

$$\tau_b = \frac{\rho_w\ V(\rho_s - \rho_w)\text{gtan}\phi}{[\frac{1}{A_p K}\int_{\frac{k_s}{2}}^{\frac{k_s}{2}+h} \frac{y}{S_G} - \frac{y-y_{int}}{S_G} \times \ln(\frac{y}{y_0})\text{dy}]^2(0.5C_D\rho_w A_p + 0.5C_L\rho_w A_s\text{tan}\phi)}. \tag{7.5}$$

7.3 Analytical results for the critical bed shear stress τ_b for each shell

The calculated critical bed shear stresses for the mussel and limpet shells in a convex upward position using equation (7.2) is summarized in Table A.1 of the Appendix. The critical bed shear stress values for the mussel and limpet shells in a convex downward position is summarized in Table A.2 of Appendix A. For the fossilized Clam shell and shell fragments, equation (7.2) is used, while equations (7.3), (7.4) and (7.5) are used for the fossilized cone, cylinder and twirl shapes, respectively. The bed shear values for these fossilized shells, in their dirty and clean states, are summarized in Tables A.3 and A.4 of Appendix A. The bed shear stress values using this analytical calculations are compared to the bed shear stress values obtained from the experiment for each of the shells. This can be seen in Figures 7.1, 7.2, 7.3, 7.4 and 7.5

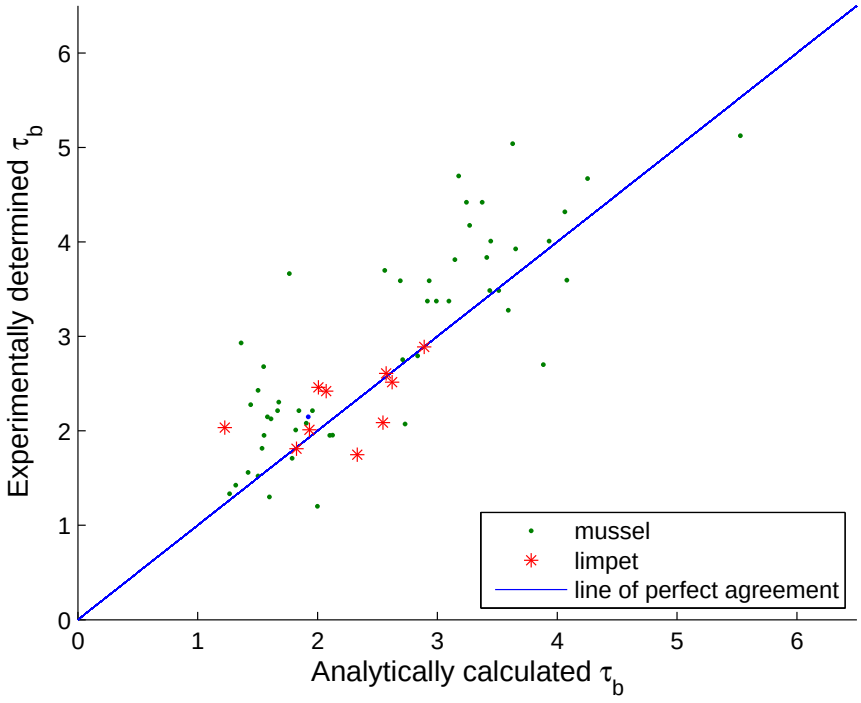

Figure 7.1. Comparison of the values of τ_b obtained using the analytical method and the experimental data for the mussel and limpet shells in a convex upward position.

The analytically calculated bed shear stress for the mussel shell underestimates the bed shear stress determined by the experiments as seen in Figure 7.1. This could be a result of the drag coefficient measured on the mussel Sample 26 having a drag coefficient higher than most of the other mussel sample shells for which the same drag coefficient was applied for. The Sample 26 of the mussel shells thus has a larger drag resistance than most of the other mussel shells in the sample set resulting in an under estimation of the bed shear stresses of the other samples. The average analytically calculated bed shear stress for the mussel shells in a convex upward position for the samples is 2.57 Pa where an average bed shear stress of 2.94 Pa was observed in the experimental determination thereof. There is an acceptable correspondence between the analytically calculated and experimentally determined bed shear stresses for the limpet shells in a convex upward position as also seen in Figure 7.1. The average analytically calculated bed shear stress for the limpet shells in a convex upward position is 2.20 Pa, and 2.26 Pa for experimental determination.

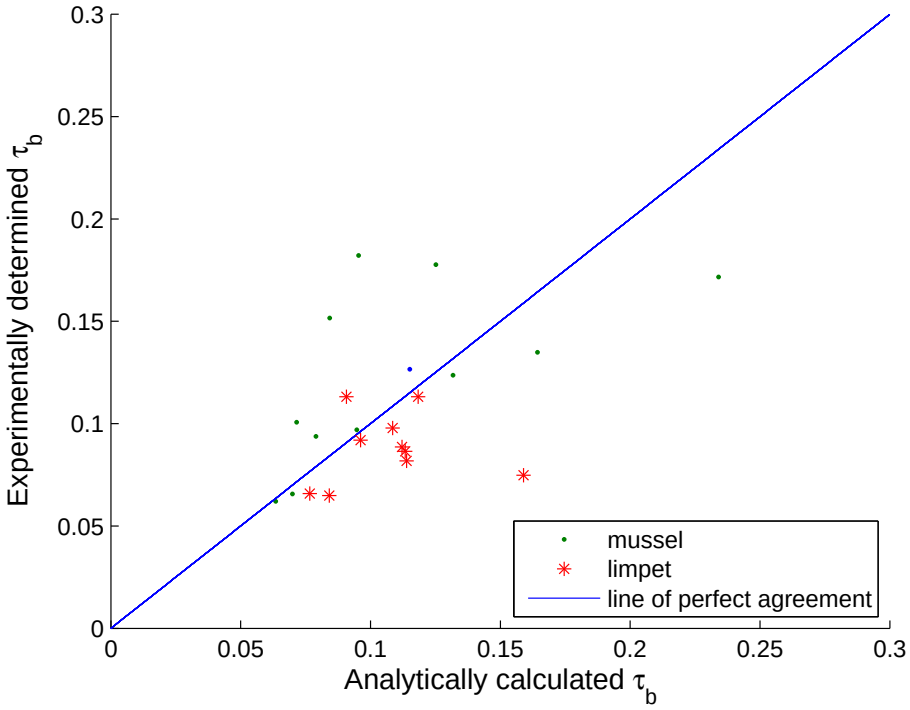

Figure 7.2. Comparison of the values of τ_b obtained using the analytical method and the experimental data for the mussel and limpet shells in a convex downward position.

The analytically determined values for the bed shear stress underestimates the bed shear stress determined from the experiments for the mussel shells in the convex downward position, as seen in Figure 7.2. This is a result of the drag coefficient determined on the Sample 26 mussel as described in the above paragraph. The average analytically calculated bed shear stress for the mussel shells in a convex downward position is 0.11 Pa, and 0.12 Pa for experimental determination. The average analytically determined bed shear stress values for the limpet shells in a convex downward position is 0.11 Pa, whereas 0.09 Pa was determined by the experimental tests. The analytical results thus overestimates the bed shear stress as observed from experiments.

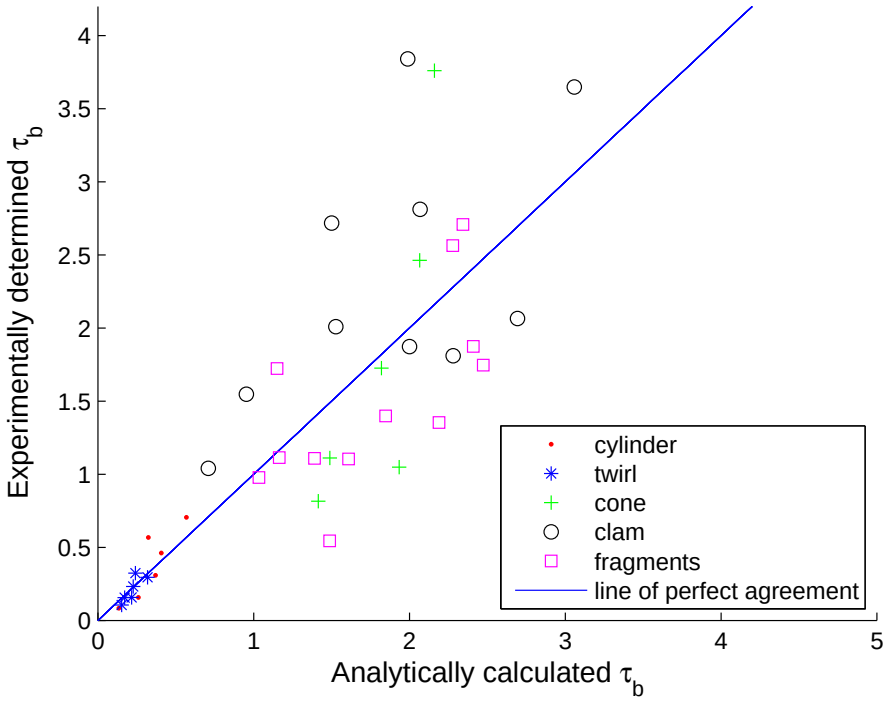

Figure 7.3. Comparison of the values of τ_b obtained using the analytical method and the experimental data for the clean fossilized shells where the clam shell is in a convex upward position.

The bed shear stress determined by the experiments and analytical calculations compared satisfactory for the fossilized shells and shell fragments as seen in Figure 7.3. The analytical average calculated bed shear stress for the cone shaped shell is 0.34 Pa where the experimental determined bed shear stress is 0.38 Pa. The twirl shaped shell has an average

bed shear stress of 0.22 Pa for the analytical method and 0.21 Pa for the experimental method. The cone shaped shell also compares well with a average bed shear stress of 1.81 Pa for the analytical method and 1.82 Pa for the experimental determination thereof. The clam shell and the shell fragments show larger differences when comparing the average bed shear stresses of the analytical and experimental estimates. The clam shell has an average bed shear stress of 1.88 Pa for the analytical method and a shear stress of 2.37 Pa for the experimental determination thereof. The shell fragments have an average bed shear stress of 1.78 Pa for the analytical method and a bed shear stress of 1.52 Pa for the bed shear stress determined by the experiments. These larger differences in bed shear stress values could be explained by the drag and lift coefficients used for the clam and flake shells. It was assumed that the clam and shell fragments have the same drag and lift coefficients as the limpet shell which could have led to these differences since their shapes are not exactly the same.

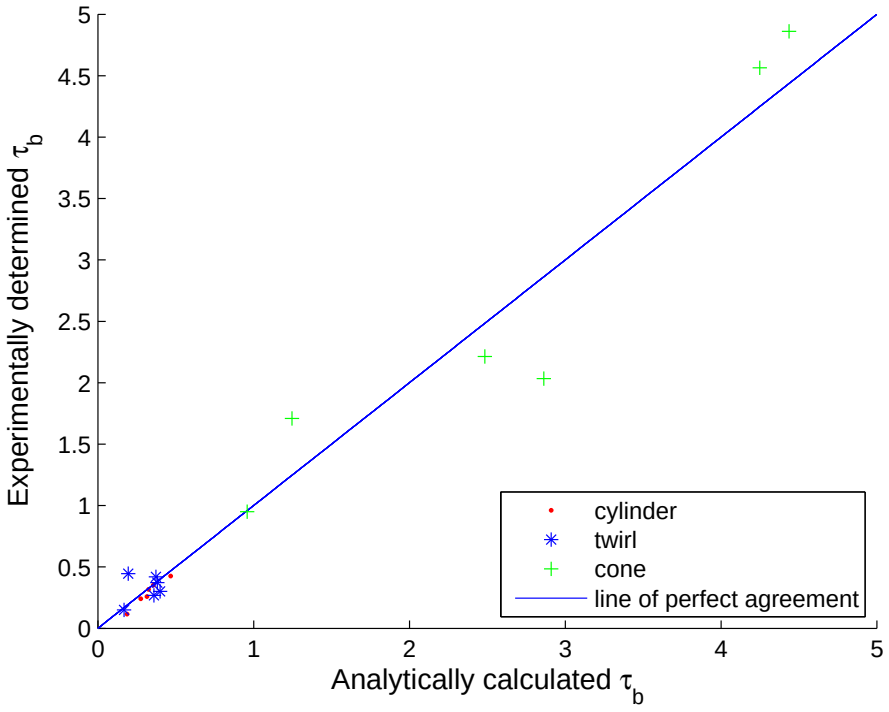

Figure 7.4. Comparison of the values of τ_b obtained using the analytical method and the experimental data for the dirty fossilized shells, excluding the clam shell.

The graphs in Figure 7.4 and 7.5 show the bed shear stresses for the fossilized shells in the dirty state determined analytically and experimentally. The analytical calculated bed shear stress data compares well with the bed shear stress values determined by the experiments. The cylinder shaped shells has an average bed shear stress value of 0.32 Pa analytically determined and an average bed shear stress of 0.28 Pa from the experiments. The average bed shear stresses for the twirl shell is 0.31 Pa and 0.33 Pa, for the cone shell it is 2.71 Pa and 2.72 Pa and for the clam shell it is 43.31 Pa and 45.93 Pa for the bed shear stress determined analytically and experimentally, respectively. The larger difference in the bed shear stresses for the clam shell can again be explained by the assumption of the shell having the same drag and lift coefficient as the limpet shell.

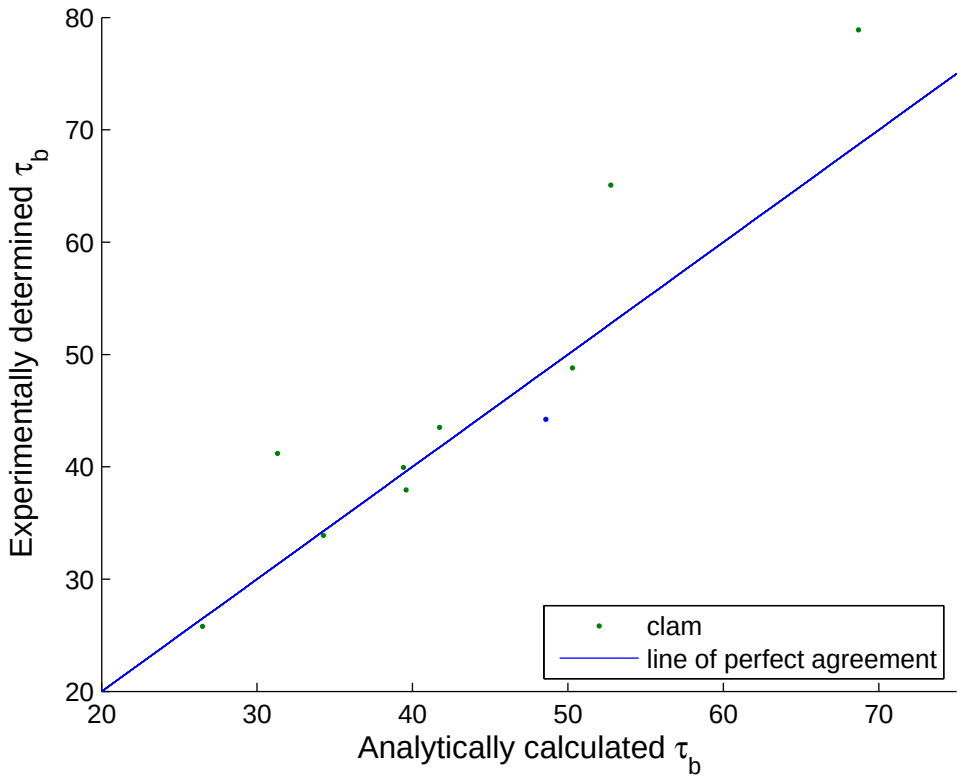

Figure 7.5. Comparison of the values of τ_b obtained using the analytical method and the experimental data for the dirty fossilized clam shell in a convex upward position.

The critical bed shear stress obtained from the experimental results for the bed roughness of $k_s = 0.3$ mm are compared to those determined by Dey [3]. Dey [3] determined values of the bed shear stress for the Coquina Clam, Cross-barred Chione and Ponderous ark. This study determined values for the bed shear stress for the mussel, limpet, fossilized clam and shell fragments. The bed shear stresses for these shells in a convex upward position are plotted relative to their shape parameter as seen in Figure 7.6

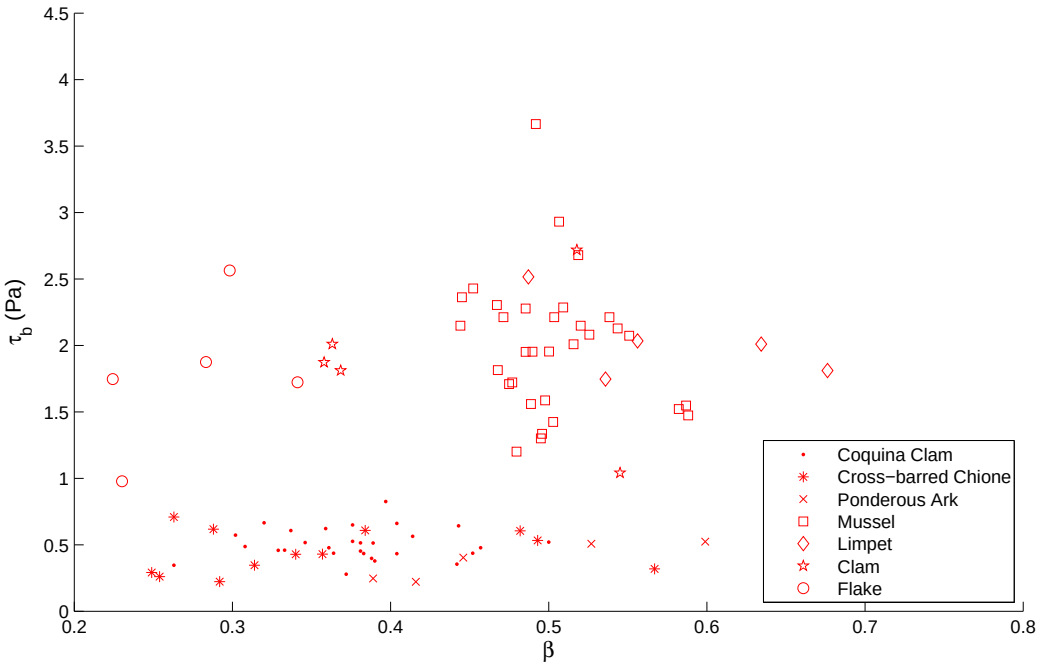

Figure 7.6. Comparison of the values of τ_b determined for Dey's shells and the shells of this study in a convex upward position relative to their shape parameter values.

The graph in Figure 7.6 clearly shows the shells in this study having much larger bed shear stresses compared to the shells of Dey [3]. The mussel shell has the largest average bed shear stress, with a value of 2.94 Pa. The limpet shell and the clam shell has an average bed shear stress value of 2.26 Pa and 2.01 Pa, respectively. The shell fragments have the smallest average bed shear stress of the shells tested in this study, with a value of 1.54 Pa. The shells tested by Dey [3], e.g. the Coqiuna Clam, Cross Barred Chione and the Ponderous Ark have average bed shear stress values of 0.51 Pa, 0.45 Pa and 0.38

Pa, respectively. According to these results, the mussel shell will be much harder to erode than the fossilized shell fragments, with a ratio of 1.91 according to the bed shear stress results. The results plotted in the graph of Figure 7.6 shows no clear relationship between the shape parameter β of the shell and the critical bed shear stress of the shell. Thus the bed shear stress of a shell can not be deduced by only taking shape parameter into account since different shell species with the same shape parameter clearly have different bed shear stresses.

The critical bed shear stresses for Dey's [3] shells as well as the mussel and limpet shells in a convex downward position are plotted relative to their shape parameter as seen in Figure 7.7

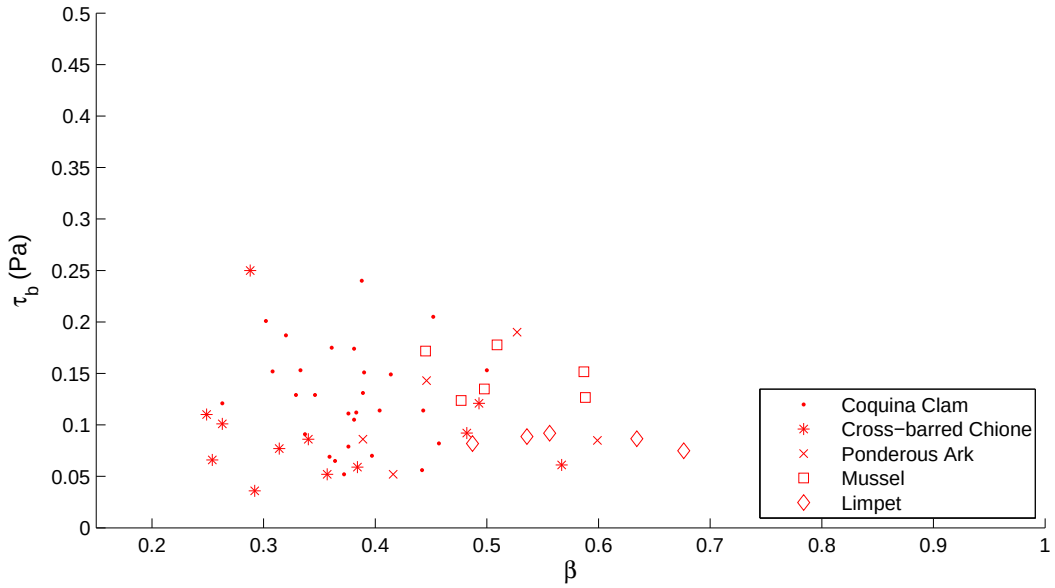

Figure 7.7. Comparison of the values of τ_b determined for Dey's shells and the shells of this study in a convex downward position relative to their shape parameter values.

The difference in bed shear stresses required for incipient motion for the shells in a convex downward position are much smaller when comparing the shells of this study and the shells of Dey's study [3], as seen in the graphs of Figure 7.7 and Figure 7.8. The shell species thus do not have a large effect on the bed shear stress when considered in the convex downward position. This can clearly be seen by considering the mussel shell in a convex

upward position, this shell had a difference in bed shear stress of 2.43 Pa compared to the Coquina Clam, when these shells are considered in the convex downward position, there is no difference in the average bed shear stress. For the shells in a convex downward postion, the mussel and limpet shells have an average bed shear stress of 0.15 Pa and 0.08 Pa, respectively. The Coquina Clam, Cross barred Chione and ponderous Ark have average bed shear stress values of 0.15 Pa, 0.09 Pa and 0.11 Pa, respectively. As for the shells in the convex upward position, no relationship is visible between the bed shear stress of the shells and their shape parameter.

The critical bed shear stresses τ_b for the mussel, limpet, clam and shell fragments are shown for the different surface roughnesses k_s in a convex upward position in Figure 7.8.

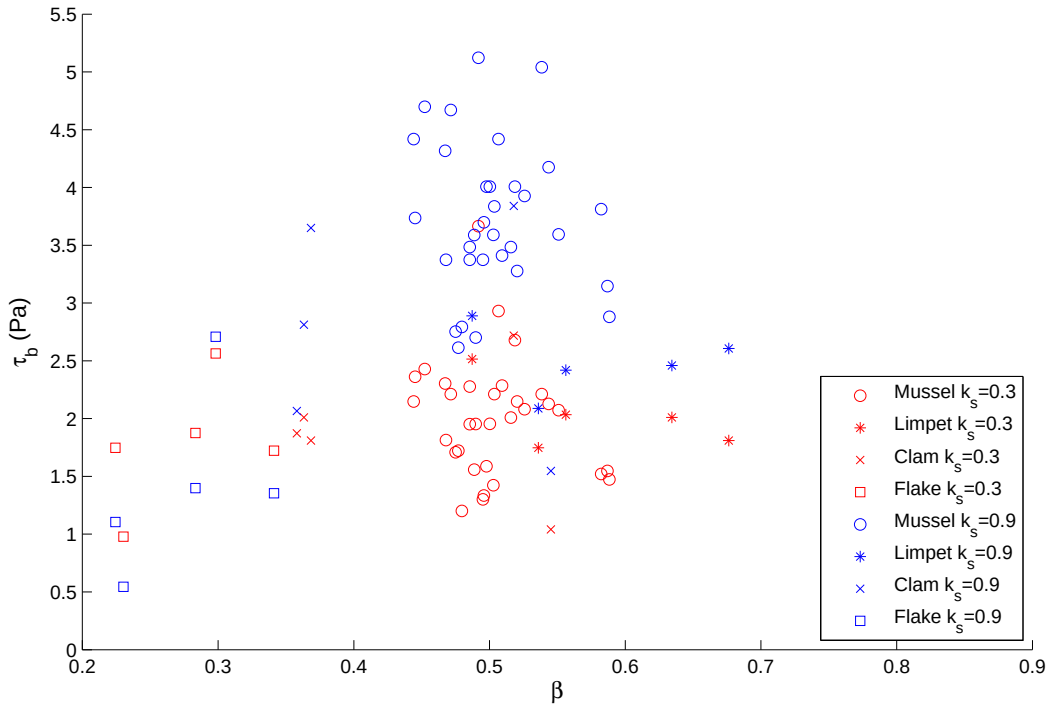

Figure 7.8. The critical bed shear stress τ_b values for various shells in a convex upward position for different surface roughness values k_s.

From the graph in Figure 7.8 it is clear that the surface roughness has an effect on the bed shear stress required by the shell for incipient motion in the cases of the mussel, limpet and clam shells. These shells require a smaller bed shear stress to move on the $k_s = 0.3$ mm bed

than on the $k_s = 0.9$ mm bed. These results make sense since the smaller sand particles with the bed roughness of $k_s = 0.3$ mm will allow a faster development of the velocity profile than the $k_s = 0.9$ mm bed. This will result in a larger drag force on the shells at the same shear stress. This is not the case for the shell fragments, as seen in Figure 7.8, where the fragments have a smaller bed shear stress on the more rough bed. This exception is explained by the nature and size of the shell fragments which when they rest on the rough bed, the fragments do not lie flat as the shells, but rather tilting, causing a larger frontal area of the fragment to be exposed in the direction of flow. This results in a larger drag force on the shell fragments than when they lie flat on the surface of the fine grain bed.

The critical bed shear stress τ_b for various fossilized shells in their clean and dirty states are shown in Figure 7.9 on the two different surface roughnesses k_s.

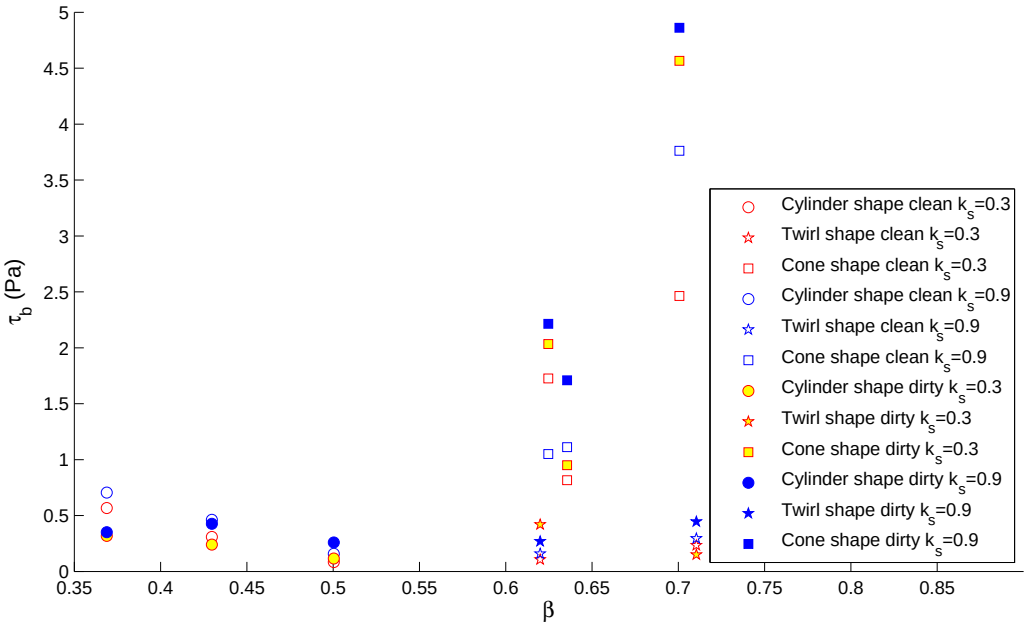

Figure 7.9. The critical bed shear stress τ_b for various fossilized shells in their clean and dirty states for different surface roughness k_s.

The graph in Figure 7.9 also shows the effect of the surface roughness on the bed shear stress required by the shell for incipient motion, as what would be expected as explained in Figure 7.8. Since the twirl and cylinder shaped shells roll on the bed rather than sliding, the effect of the extra weight of the shell in the dirty state has a much less effect than

the shells sliding on the bed at incipient motion. The graph shows almost no increase in the bed shear stress for the cylinder and twirl shaped shells in their dirty and clean states when compared to the cone shaped shell which slides at incipient motion. The same is true for the fossilized clam shell which is not plotted on the graph due to the large difference of the bed shear stress in its clean and dirty state. The clam shell also slides over the bed at incipient motion.

The scatter of the graphs in Figure 7.1, 7.2, 7.3, 7.4 and 7.5 is partly explained by the fact that the exact moment of incipient motion is difficult to detect due to the nature of the experiments. There will thus always be a variation of the results when an experimental run is repeated. Table 7.1 shows the critical bed shear stress of 5 repeated experimental runs on the same mussel and limpet shell lying on the same bed in a convex upward position.

Table 7.1. Repeated experimental runs on the mussel and limpet shell.

Shell:	Mussel	Limpet
Experimental run	τ_b	τ_b
Run 1	1.3482	2.5070
Run 2	1.7112	2.1895
Run 3	2.4122	1.6148
Run 4	2.1281	1.7861
Run 5	1.7718	2.3310

The standard errors for the mussel and the limpet shell in a convex upward position are 0.183 and 0.167, respectively, where the average values were chosen as the exact values. Another factor which could add to the scatter of the results the inaccuracy of the drag and lift coefficients determined with the strain gauge. Table 7.2 shows the calculated drag coefficients of a perfect cube at the condition of incipient motion. It is clear that variations of the drag coefficient exist when measuring it with the strain gauge. The standard error for these 5 experimental runs is 0.045. The average drag coefficient calculated by using these different experimental runs for the cube is 1.07, where a drag coefficient of 1.05 would have been expected. Since this cube has a smooth surface, the angle of friction could be determined more accurately, respective values of $34°, 34°, 34°, 35°$ and $36°$ were measured, and thus an average of $34.6°$ was found. The frontal area of the cube is easily determined,

with no variations as in the case of the shells, all variables used are shown in Table A.8 of Appendix A. Even under almost perfect conditions as these, the analytically determined bed shear stress for the cube is 0.0143 Pa where the experimentally determined bed shear stress is 0.015. A percentage error of about 5% is present.

Table 7.2. The calculated drag coefficients determined from repeated experimental runs on a perfect cube.

Experimental run	C_D
Run 1	0.93
Run 2	0.95
Run 3	1.09
Run 4	1.15
Run 5	1.06
Run 6	1.22

It is thus clear that variations do occur, and the results should be viewed as an average over a number of observations rather than an individual result. The errors are also due to the typical shape of the shells that makes it a difficult task to have a foolproof model to determine the bed shear stress, since every shell is slightly different.

Chapter 8

The Shields parameter and grain Reynolds number

The usual way of representing the incipient motion of particles is to use a dimensionless number called the Shields parameter [20]. The Shields parameter is tied to the gravitational influences that tend to keep a particle at rest. The grain Reynolds number relates to the viscous effects that tend to initiate the motion of the particle [21], [22]. The Shields diagram empirically shows how the dimensionless critical shear stress, known as the Shields parameter, is a function of the particle Reynolds number. The Shields parameter has been utilized in a variety of sediment transport procedures. This work included sediment such as coal, amber cuttings, crushed barite, and crushed granite fragments [23]. In this chapter, the experimental results of the mussel, limpet, fossilized clam and shell fragments in a convex upward position is translated into Shields parameters as done by Ramsdell et al. [5] on the experimental results of Dey [3]. These results are then compared to each other.

8.1 Shields parameter θ

The Shields parameter θ measures the relative importance of the stabilizing hydrodynamic force and the destabilizing gravity force. The stabilizing hydrodynamic force is expressed as $\tau_b d^2$. The stabilizing gravity force is expressed as $(\rho_s - \rho)\, g d^3$, which is the apparent weight of the grain, where d is the grain diameter of the particle, ρ_s and ρ is the density of the solid and fluid, respectively.

The Shields parameter θ is expressed as a ratio between the hydrodynamic force and the stabilizing gravity force:

$$\theta = \frac{\tau_b}{(\rho_s - \rho)\, gd}. \tag{8.1}$$

In this study, the diameter d is assumed to be the same as the bed roughness k_s and the characteristic diameter D_{50}, as done in the study of Dey [3] and Ramsdell et al. [5]. Ramsdell et al. [5] suggested that the Shields parameter is a shear stress divided by a normal stress and in the case of shells, the normal stress depends on the thickness of the shell and not the size. Thus for the calculation of the Shields parameter by equation (8.1) for the shells, the grain diameter d is substituted with the thickness t_c of the shell. The Shields values calculated for each sample shell on the different beds using this method of applying equation (8.1) is summarized in Table 8.1, where the density and bed shear stress of the shell is used as determined from the experiments.

From the results in Table 8.1 it is seen that the shells that require larger bed shear stresses for incipient motion have larger Shields values as would be expected when compared to the Shields values from sand grain particles. The average Shields values determined by Ramsdell et al. [5] from the experiments of Dey [3] and the average Shields values of each shell in Table 8.1 are summarized in Table 8.2.

The average values in Table 8.2 also show that the shells that require larger bed shear stresses for incipient motion have larger Shields values. This is not true for the shell fragments and will be further investigated in Section 8.3.

Table 8.1. The Shields values calculated from the thickness t_c.

Sample	Shields value θ		Sample	Shields value θ	
	$D_{50} = 0.3\,\text{mm}$	$D_{50} = 0.9\,\text{mm}$		$D_{50} = 0.3\,\text{mm}$	$D_{50} = 0.9\,\text{mm}$
Mussel 1	0.138	0.210	Mussel 25	0.314	0.473
Mussel 2	0.125	0.173	Mussel 26	0.070	0.121
Mussel 3	0.125	0.257	Mussel 27	0.158	0.308
Mussel 4	0.156	0.292	Mussel 28	0.166	0.337
Mussel 5	0.142	0.300	Mussel 29	0.093	0.234
Mussel 6	0.077	0.179	Mussel 30	0.111	0.168
Mussel 7	0.150	0.259	Mussel 31	0.154	0.230
Mussel 8	0.122	0.196	Mussel 32	0.144	0.228
Mussel 9	0.129	0.241	Limpet 1	0.058	0.084
Mussel 10	0.143	0.249	Limpet 2	0.135	0.155
Mussel 11	0.093	0.241	Limpet 3	0.108	0.132
Mussel 12	0.139	0.241	Limpet 4	0.112	0.134
Mussel 13	0.183	0.280	Limpet 5	0.154	0.183
Mussel 14	0.261	0.365	Clam 1	0.077	0.156
Mussel 15	0.153	0.315	Clam 2	0.092	0.102
Mussel 16	0.148	0.280	Clam 3	0.129	0.181
Mussel 17	0.215	0.322	Clam 4	0.116	0.164
Mussel 18	0.131	0.329	Clam 5	0.067	0.099
Mussel 19	0.125	0.288	Fragment 1	0.120	0.090
Mussel 20	0.223	0.431	Fragment 2	0.221	0.174
Mussel 21	0.228	0.447	Fragment 3	0.314	0.175
Mussel 22	0.163	0.408	Fragment 4	0.224	0.142
Mussel 23	0.143	0.396	Fragment 5	0.165	0.174
Mussel 24	0.237	0.539	Fragment 6	0.358	0.356

Table 8.2. The average Shields values calculated from the thickness t_c and the critical bed shear stress from the shells of Dey (2003) and Table 8.1.

Sample	Shields value θ		
	$D_{50} = 0.3\,\text{mm}$	$D_{50} = 0.8\,\text{mm}$	$D_{50} = 0.9\,\text{mm}$
Coquina Clam	0.023	0.028	
Cross Barred Chione	0.033	0.038	
Ponderous Ark	0.009	0.013	
Mussel	0.155		0.292
Limpet	0.113		0.137
Clam	0.096		0.140
Fragment	0.234		0.185

8.2 Grain Reynolds number R_*

The grain Reynolds number is expressed as follow:

$$R_* = \frac{u_* D_{50}}{\nu}, \tag{8.2}$$

where u_* is the shear velocity, ν is the kinematic viscosity of the fluid and D_{50} is the characteristic diameter of the sand particles on the bed. The grain Reynolds number is calculated using the shear velocity at incipient motion of the shell and the characteristic grain diameter of the bed. These values are summarized in Table A.9 and Table A.10 in Appendix A for Dey's [3] shells and for the sample shells for the different bed roughnesses, respectively. The grain Reynolds number for the grains on the bed is calculated with the shear velocity of the shells to compare when the shells erode relative to the sand bed with no shells since the grain Reynolds number for the grains is already known from previous studies.

The ratios between the thickness t_c of the shells and the grain roughness k_s of the bed for the sample shells is determined and summarized in Table A.11 in Appendix A. These ratios will be used to compare when the shells erode relative to the sand bed with no shells. The thicknesses t_c of the shells are summarized in Tables 3.1 and 3.2. The bed roughness k_s is assumed to be the same as the characteristic diameter D_{50} of the grains.

8.3 Non-uniform particle distribution

In this study, the particles lying on a bed, e.g. the shells, have a different diameter than the particles of the bed itself. The bed roughness diameter may be smaller or larger than the particle's diameter that is lying on the bed. Figure 8.1 shows the Shields curves for particles that have a different grain diameter than the bed. The non-uniform particles with a diameter d, will be related to the shells by substituting the diameter d by the thickness of the shell t_c, as done by Ramsdell et al. [5], thus in Figure 8.1, the bed's grain roughness is $D_{50} = k_s$, where $d = t_c$, when considering shells lying on a bed of sand. To interpret the graph in Figure 8.1, the grain Reynolds number must be determined. The grain Reynolds numbers for each case of the shells was determined in Section 8.2 and summarized in Ta-

bles A.9 and A.10 of Appendix A.

To determine the Shields value using the graph in Figure 8.1, the vertical through the grain Reynolds number is taken until it meets the curve of the ratio $\frac{d}{k_s}$ under consideration.

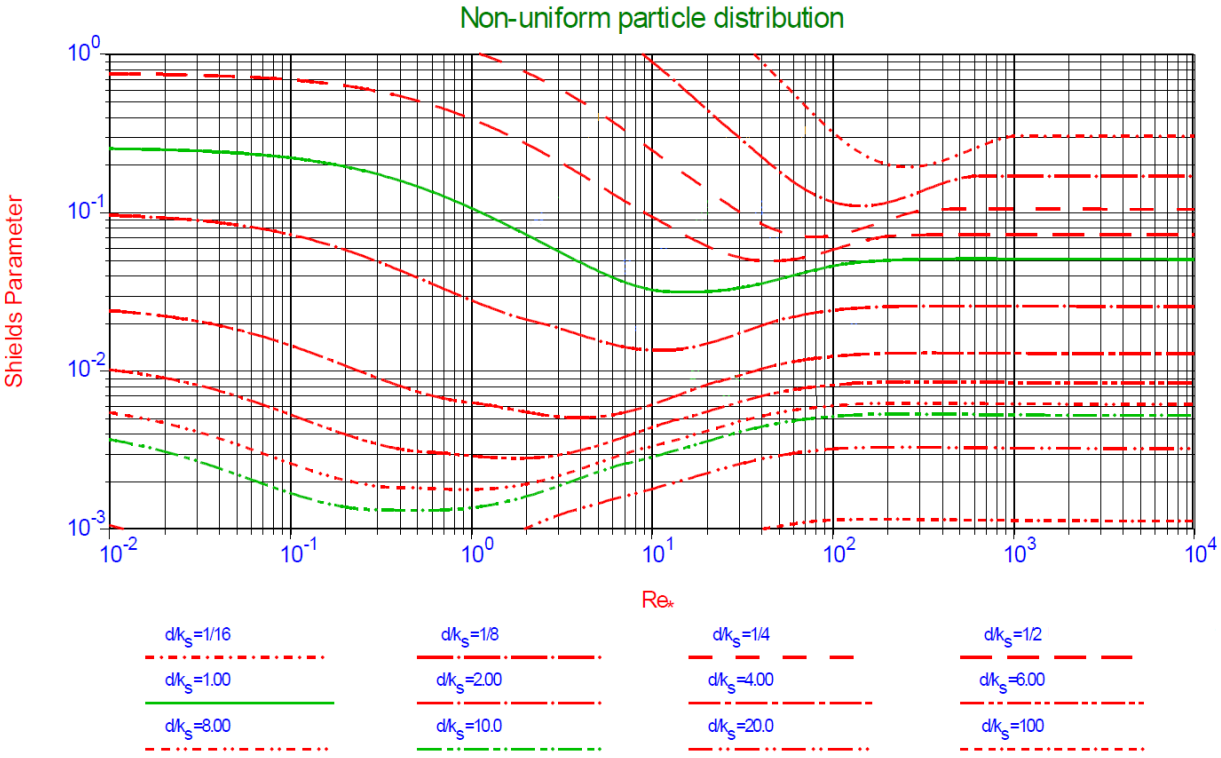

Figure 8.1. The Shields parameter for non-uniform particle distributions, Graph from Miedema (2011).

The ratios between the thickness d of the shells and the grain roughness k_s of the bed is determined and is summarized in Table A.11 of Appendix A for the sample shells. The average grain Reynolds numbers and $\frac{d}{k_s}$ ratios for all shells are summarized in Table 8.3. The corresponding Shields values are then found on the vertical axes. By using this method, all the corresponding Shields values based on the $\frac{d}{k_s}$ ratio is found. This is summarized in Table 8.4.

Table 8.3. The average grain Reynolds number and the $\frac{d}{k_s}$ ratio for the shell samples.

D_{50}:	0.3 mm	0.9 mm	0.3 mm	0.9 mm
Sample	Grain Reynolds number R_*		$\frac{d}{k_s}$ ratio	
Mussel	13.300	54.598	2.93	0.98
Limpet	13.427	44.742	4.17	1.39
Clam	12.866	46.699	4.20	1.40
Fragment	12.060	32.323	1.89	0.63
D_{50}:	0.3 mm	0.8 mm	0.3 mm	0.8 mm
Sample	Grain Reynolds number R_*		$\frac{d}{k_s}$ ratio	
Coqiuna Clam	6.710	19.780	5.33	2.00
Cross Barred Chione	6.240	17.510	3.76	1.41
Ponderous Ark	5.760	18.460	8.97	3.36

Table 8.4. The Shields values θ and the Shields values θ_R determined by the ratio $\frac{d}{k_s}$.

D_{50}:	0.3 mm	0.3 mm	0.9 mm	0.9 mm
Sample	θ	θ_R	θ	θ_R
Mussel	0.1549	0.0090	0.2918	0.04
Limpet	0.1132	0.0065	0.1373	0.028
Clam	0.0964	0.0060	0.1405	0.029
Fragment	0.2337	0.0150	0.1850	0.048
D_{50}	0.3 mm	0.3 mm	0.8 mm	0.8 mm
Sample	θ	θ_R	θ	θ_R
Coqiuna Clam	0.0225	0.0045	0.0277	0.015
Cross Barred Chione	0.0333	0.0055	0.0378	0.02
Ponderous Ark	0.0086	0.0028	0.0129	0.008

Comparing the Shields values of the shells determined by equation (8.1) to the Shields

values for sand particles with a diameter equal to the thickness of the shell using the non-uniform particle distribution plot, factors exist. The mussel shell requires a Shields value 17.2 times larger than the Shields value of a sand particle with the same diameter d for the surface with a bed roughness of $k_s = 0.3$ mm. The limpet shell requires a Shields value 17.4 times larger, the clam shell 16.1 times larger and the shell fragments 15.6 times larger for a bed roughness of $k_s = 0.3$ mm. For the bed roughness of $k_s = 0.9$ mm, the Shields value for the mussel is 7.3 times larger, for the limpet it is 4.9 times larger, for the clam it is 4.8 times larger and for the shell fragments it is 3.9 times larger than the Shields value corresponding to the grain size with the diameter equal to the thickness of the shell. It is thus clear that the shells require larger Shields values than the corresponding sand grains. The exact ratios of these Shields values depend on the type of shells. It is seen that the ratio is larger in the case of shells laying on a bed with finer sand particles than on the bed with rough particles. The ratios from the measurements of Dey's shells show the same trend.

Another way to compare how the shells react differently than that of the sand, is to analyze the shear stresses that occur to erode the shells and the shear stresses that occur to erode the sand bed. The average bed shear stresses required for incipient motion of the sample shells and Dey's [3] shells for each bed is summarized in Table 8.5.

Table 8.5. The average shear stresses for the sample shells as well as Dey's shells for the different beds.

D_{50}:	0.3 mm	0.9 mm
Sample	bed shear stress τ_b (Pa)	bed shear stress τ_b (Pa)
Mussel	2.006	3.729
Limpet	2.023	2.493
Clam	1.890	2.783
Fragment	1.667	1.370
D_{50}:	0.3 mm	0.8 mm
Sample	bed shear stress τ_b (Pa)	bed shear stress τ_b (Pa)
Coqiuna Clam	0.507	0.615
Cross Barred Chione	0.447	0.498
Ponderous Ark	0.380	0.547

It is known that the Shields values for the sand on the bed surfaces used are 0.035 [5]. Since the characteristic diameter D_{50} of the grains is known, the bed shear stresses can be calculated for each of the sand surfaces using equation (8.1), where $d = D_{50}$. The calculated bed shear stresses for each of the sand surfaces are summarized in Table 8.6

Table 8.6. The critical bed shear stresses of the grains for the different sand surfaces.

D_{50} :	0.3 mm	0.8 mm	0.9 mm
Bed shear stress (Pa):	0.17	0.45	0.51

The ratios between the shear stresses required to erode the shells and the shear stresses required eroding the beds are shown in Table 8.7.

Table 8.7. The ratios between the bed shear stresses of the bed and shells.

D_{50}:	$k_s = 0.3$ mm	$k_s = 0.9$ mm
Sample	$\frac{\tau_b\ shell}{\tau_b\ sand}$ ratio	$\frac{\tau_b\ shell}{\tau_b\ sand}$ ratio
Mussel	11.80	7.31
Limpet	11.90	4.89
Clam	11.12	5.46
Fragment	9.81	2.69
D_{50}:	$k_s = 0.3$ mm	$k_s = 0.8$ mm
Sample	$\frac{\tau_b\ shell}{\tau_b\ sand}$ ratio	$\frac{\tau_b\ shell}{\tau_b\ sand}$ ratio
Coqiuna Clam	3.41	1.6
Cross Barred Chione	3.59	1.53
Ponderous Ark	2.18	1.24

The ratios in Table 8.7 shows that for the shells used in this study require an average bed shear stress that is 11.16 times larger than the bed shear stress required to erode the sand bed with a characteristic diameter $D_{50} = 0.3$ mm and a average bed shear stress 5.09 times larger for the bed with a characteristic diameter $D_{50} = 0.9$ mm. Since the smaller

sand particles of the bed require smaller shear stresses to initiate incipient motion, the ratios for the shells on the finer sand beds will be smaller. The same trend is seen in the bed shear stress ratios for Dey's shells. Dey's shells require a average bed shear stress 3.06 times larger than the sand bed with a characteristic diameter of $D_{50} = 0.3$ mm and a average bed shear stress 1.46 times larger than the sand bed with a characteristic diameter of $D_{50} = 0.9$ mm.

Chapter 9

Discussion and conclusions

9.1 Discussion

From the results of this study it may be concluded that the mussel and limpet shells require larger bed shear stresses to initiate incipient motion than the other sample shells. They are thus also more difficult to erode than the shells investigated by Dey [3]. The mussel and limpet shells, when considered on the same type of bed as the shells of Dey [3], require an average bed shear stress 4.53 times larger than the shells of Dey [3] when considered in a convex upward position. When these shells are considered in a convex downward position, the shells require an average bed shear stress 1.02 times smaller than that of Dey [3]. The shells in this study and the shells of Dey [3] are thus almost exactly the same when considered in this position. The difference in these results could be explained by the fact that the mussel and limpet shells have sharper edges than the Coquina Clam, Cross Barred Chione and Ponderous Ark shells. Thus for the shells in a convex downward position, the sharper edges causes larger friction between the bed and the shell.

The bed shear stress required to initiate incipient motion of the fossilized shells showed no significant difference to the non fossilized shells. The shells in their dirty and clean states also showed no significant differences when the mode of transport was rolling, as was the case for the cylindrical and twirl shaped shells. This was not the case for the shells when the mode of transport was sliding; as for the clam shell required a bed shear stress 23.25 larger in the dirty than in the clean state. However, it was observed that the shells in their

dirty states did get cleaned under the flow of water when experiments were conducted, thus the shells would not always stay dirty when exposed to water flow and the dirt would erode.

Ramsdell et al. [5] suggested that the ratio between the critical bed shear stress of the shells and the critical bed shear stress of the sand will approach 1 if the sand particles have a diameter d matching the thickness t_c of the shell. This may even become smaller than 1 if the sand particles are larger than the shells. The results from the shells tested by Dey which include the Coquina Clam, Cross Barred Chione and Ponderous Ark, indicate that this statement is plausible.

The mussel shell and fossilized shell fragments from this study have a ratio $\frac{d}{k_s} = 0.98$ and $\frac{d}{k_s} = 0.63$, respectively, as shown in Table 8.3 for the bed with a characteristic diameter $D_{50} = 0.9$ mm. The mussel shell thus has a ratio $\frac{d}{k_s}$ approaching 1 but has an average bed shear ratio $\frac{\tau_b\ shell}{\tau_b\ sand} = 7.31$. The fossilized shell fragments have a ratio $\frac{d}{k_s} = 0.63$ which is smaller than 1, but has an average bed shear ratio $\frac{\tau_b\ shell}{\tau_b\ sand} = 2.69$.

The results obtained in this study from the mussel, limpet, fossilized clam and shell fragments indicate that the assumption made by Ramsdell et al. [5] which states that the ratio between the critical bed shear stress of the shells and the critical bed shear stress of the sand will approach 1 if the sand particles will have a diameter d matching the thickness t_c of the shell does not hold true, as seen in the case of the mussel shell. The mussel shell has a thickness ratio of 0.98 but a bed shear stress ratio of 7.31. The assumption that this ratio will become smaller than 1 if the sand particles are larger than the shells also does not hold true when considering the case of the fossilized shell fragments as mentioned in the above paragraph, which have a thickness ratio less that 1 but has a bed shear stress ratio of 2.69.

Since the assumption of Ramsdell et al. [5] does not hold true for all the shells, it is not possible to relate the Shields value of a sand grain to that of a shell, e.g. the thickness t_c of the shell to the diameter d of a sand grain, as was done using equation (8.1). As a result of this, the Shields parameter determined from the non-uniform particle distribution graph in Figure 8.1 using the thickness ratios will not be accurate since the Shields value of

a shell and the Shields value of a grain with a diameter equal to that of the shell thickness are not the same. This is further explained by the fact that the Shields parameter is defined by the ratio of the destabilizing hydrodynamic force and the destabilizing gravity force and not necessarily the ratio of the shear force and normal force as suggested by Ramsdell et al. [5]. The denominator in equation (8.1) rather represents the buoyancy force than the normal force, and thus the diameter d in the denominator is relevant to the volume of the grain where the thickness t_c of the shell is not.

9.2 Summary

In the present study, the erosion characteristics of shells and shell fragments are investigated. When shells settle, they settle like leaves, where the biggest cross section is exposed to the drag, unlike when it is flat on the bed where the smaller cross section is exposed to the direction of flow. The settling velocity of shells are thus lower than the velocity required to make them erode. A model is presented to determine the critical bed shear stress of various shells at incipient motion lying flat on a horizontal sand bed. This model makes use of the hydrodynamical forces, where drag and lift forces are taken into consideration.

The mussel and limpet shells are investigated, as well as various shapes of fossilized shells and fragments, in their dirty and clean states. These results are compared to results found in literature. Experiments were conducted in an open channel to determine critical bed shear stresses for incipient motion of the shells using Vanoni's side-wall correction. The lift and drag forces of the mussel and limpet shells are also determined under the flow of water using a strain gauge. The experimental data is compared to the data obtained by the analytical model. The Shields parameter is used in an attempt to relate the erosion characteristics of the shells to non-uniform sand grains on a bed.

Appendix A

Table A.1. The bed shear stress for the mussel and limpet shells in a convex upward position.

	bed shear stress for convex upward position	
Sample	Fine grained surface (d =0.3mm)	Rough grained surface (d =0.9mm)
Mussel 1	1.923	3.591
Mussel 2	2.103	3.884
Mussel 3	2.125	3.932
Mussel 4	1.677	4.063
Mussel 5	1.958	4.253
Mussel 6	1.999	2.835
Mussel 7	1.845	3.412
Mussel 8	1.789	2.710
Mussel 9	1.537	3.096
Mussel 10	1.818	3.437
Mussel 11	1.598	2.992
Mussel 12	1.553	2.917
Mussel 13	1.443	3.512
Mussel 14	1.764	5.528
Mussel 15	1.582	3.373
Mussel 16	1.907	3.653
Mussel 17	1.550	3.445
Mussel 18	1.317	2.690
Mussel 19	1.420	2.931
Mussel 20	1.503	3.177
Mussel 21	1.611	3.269
Mussel 22	1.503	3.146
Mussel 23	1.266	2.561
Mussel 24	1.666	3.628
Mussel 25	1.362	3.243
Mussel 26	2.731	4.081
Mussel 27	1.539	2.958
Mussel 28	1.689	3.227
Mussel 29	2.305	4.285
Mussel 30	1.882	2.853
Mussel 31	1.731	3.248
Mussel 32	2.244	3.859
Limpet 1	1.824	2.572
Limpet 2	2.623	2.890
Limpet 3	1.933	2.008
Limpet 4	2.331	2.545
Limpet 5	1.227	2.072

Table A.2. The bed shear stress for the mussel and limpet shells in a convex downward position.

	bed shear stress for convex downward position	
Sample	Fine grained surface (d =0.3mm)	Rough grained surface (d =0.9mm)
Mussel 27	0.115	0.064
Mussel 28	0.084	0.070
Mussel 29	0.164	0.095
Mussel 30	0.132	0.079
Mussel 31	0.125	0.072
Mussel 32	0.234	0.095
Limpet 1	0.159	0.084
Limpet 2	0.114	0.118
Limpet 3	0.113	0.091
Limpet 4	0.112	0.108
Limpet 5	0.096	0.077

Table A.3. The bed shear stress for the shells in their clean states.

	Bed shear stress	
Sample	Fine grained surface (d =0.3mm)	Rough grained surface (d =0.9mm)
Cylinder 1	0.325	0.568
Cylinder 2	0.370	0.407
Cylinder 3	0.135	0.261
Twirl 1	0.227	0.319
Twirl 2	0.172	0.241
Twirl 3	0.153	0.217
Cone 1	2.066	2.161
Cone 2	1.415	1.489
Cone 3	1.820	1.934
Clam 1	2.281	3.059
Clam 2	2.000	2.694
Clam 3	1.527	2.069
Clam 4	1.501	1.989
Clam 5	0.710	0.954
Fragment 1	2.410	1.848
Fragment 2	1.150	2.190
Fragment 3	1.034	1.487
Fragment 4	2.474	1.609
Fragment 5	2.279	2.344
Fragment 6	1.165	1.390

Table A.4. The bed shear stress for the shells in their dirty states.

	Bed shear stress	
Sample	Fine grained surface (d =0.3mm)	Rough grained surface (d =0.9mm)
Cylinder 1	0.325	0.356
Cylinder 2	0.276	0.467
Cylinder 3	0.188	0.315
Twirl 1	0.168	0.195
Twirl 2	0.400	0.381
Twirl 3	0.373	0.360
Cone 1	4.249	4.437
Cone 2	0.958	1.247
Cone 3	2.862	2.483
Clam 1	48.580	50.299
Clam 2	26.492	34.269
Clam 3	41.737	39.421
Clam 4	52.758	68.694
Clam 5	31.313	39.588

Table A.5. The average angle of friction ϕ for the fossilized shells in their clean and dirty states.

	Angle of friction ϕ			
	clean state		dirty state	
Sample	d = 0.3 mm	d = 0.9 mm	d = 0.3 mm	d = 0.9 mm
Cylinder 1	32.5	42.0	35.1	44.4
Cylinder 2	32.5	35.5	35.0	38.2
Cylinder 3	19.5	16.5	22.3	19.2
Twirl 1	19.4	19.4	16.6	16.5
Twirl 2	19.4	19.4	16.5	16.3
Twirl 3	19.4	19.4	16.7	16.5
Cone 1	41.5	44.5	41.9	44.9
Cone 2	41.5	44.5	41.9	45.0
Cone 3	41.5	44.5	41.6	44.5
Clam 1	50.5	59.9	52.8	62.1
Clam 2	50.5	59.9	52.9	62.3
Clam 3	50.5	59.9	52.9	62.2
Clam 4	50.5	59.9	52.6	62.0
Clam 5	50.5	59.9	52.8	62.2

Table A.6. The average angle of friction ϕ for the mussel, limpet and shell fragments in a convex upward position.

Sample	Angle of friction ϕ		Sample	Angle of friction ϕ	
	d = 0.3 mm	d = 0.9 mm		d = 0.3 mm	d = 0.9 mm
Fragment 1	38.0	44.1	Mussel 17	45.2	55.2
Fragment 2	38.0	44.5	Mussel 18	45.2	55.1
Fragment 3	39.0	45.5	Mussel 19	45.2	55.1
Fragment 4	35.0	37.8	Mussel 20	45.2	55.2
Fragment 5	41.5	44.3	Mussel 21	45.2	55.1
Fragment 6	41.0	44.1	Mussel 22	45.2	55.1
Mussel 1	45.2	55	Mussel 23	45.2	55.1
Mussel 2	45.2	55	Mussel 24	45.2	55.2
Mussel 3	45.2	55	Mussel 25	45.2	55.3
Mussel 4	45.2	55.3	Mussel 26	45.2	54.7
Mussel 5	45.2	55.2	Mussel 27	45.2	55
Mussel 6	45.2	54.6	Mussel 28	45.2	55
Mussel 7	45.2	55	Mussel 29	45.2	55
Mussel 8	45.2	54.7	Mussel 30	45.2	54.7
Mussel 9	45.2	55.1	Mussel 31	45.2	55
Mussel 10	45.2	55	Mussel 32	45.2	54.9
Mussel 11	45.2	55	Limpet 1	44.3	44.3
Mussel 12	45.2	55	Limpet 2	44.8	44.5
Mussel 13	45.2	55.3	Limpet 3	44.8	44.5
Mussel 14	45.2	55.5	Limpet 4	44.8	44.5
Mussel 15	45.2	55.2	Limpet 5	44.8	45
Mussel 16	45.2	55			

Table A.7. The average angle of friction ϕ for the mussel, limpet shells in a convex downward position.

Sample	Angle of friction ϕ	
	d = 0.3 mm	d = 0.9 mm
Mussel 27	28	31.5
Mussel 28	29	31.5
Mussel 29	28	31.5
Mussel 30	28	31.5
Mussel 31	28	31.5
Mussel 32	25	31.5
Limpet 1	25.3	28.2
Limpet 2	25.5	28.4
Limpet 3	27.5	28.4
Limpet 4	26	28.4
Limpet 5	25	28.5

Table A.8. The variables used to determine the critical bed shear stress experimentally and analytically for the cube.

A_p (m^2)	0.0009
ρ (kg/m^3)	1216.54
h (m)	0.1935
U (m/s)	0.0568
a (m)	0.03
b (m)	0.03
c (m)	0.03
ϕ (°)	34.6
k_s (m)	0.0003
C_D	1.05
C_L	0

Table A.9. The average grain Reynolds number values calculated for the different bed roughness and the critical bed shear stress from the shell samples of Dey (2003).

Sample	Grain Reynolds number	
	$D_{50} = 0.3\,\text{mm}$	$D_{50} = 0.8\,\text{mm}$
Coquina Clam	6.710	19.780
Cross Barred Chione	6.240	17.510
Ponderous Ark	5.760	18.460

Table A.10. The grain Reynolds number values calculated for the different bed roughness and the critical bed shear stress from the shell samples.

Sample	Grain Reynolds number		Sample	Grain Reynolds number	
	$D_{50} = 0.3\,\text{mm}$	$D_{50} = 0.9\,\text{mm}$		$D_{50} = 0.3\,\text{mm}$	$D_{50} = 0.9\,\text{mm}$
Mussel 1	13.866	51.367	Mussel 25	16.193	59.652
Mussel 2	13.219	46.640	Mussel 26	13.618	53.804
Mussel 3	13.224	56.809	Mussel 27	11.482	48.171
Mussel 4	14.356	58.968	Mussel 28	11.765	50.341
Mussel 5	14.071	61.333	Mussel 29	11.916	56.809
Mussel 6	10.368	47.432	Mussel 30	12.413	45.886
Mussel 7	14.071	55.580	Mussel 31	14.300	52.410
Mussel 8	12.366	47.090	Mussel 32	14.537	54.856
Mussel 9	12.740	52.130	Limpet 1	12.728	45.823
Mussel 10	13.408	52.971	Limpet 2	15.002	48.232
Mussel 11	10.787	52.130	Limpet 3	13.411	44.503
Mussel 12	13.213	52.130	Limpet 4	12.503	41.005
Mussel 13	14.274	52.971	Limpet 5	13.490	44.144
Mussel 14	18.111	64.233	Clam 1	12.727	54.212
Mussel 15	13.866	59.652	Clam 2	12.945	40.782
Mussel 16	13.646	56.233	Clam 3	13.411	47.591
Mussel 17	15.482	56.809	Clam 4	15.594	55.613
Mussel 18	11.287	53.766	Clam 5	9.652	35.297
Mussel 19	11.811	53.760	Fragment 1	12.953	33.558
Mussel 20	14.742	61.511	Fragment 2	12.417	33.016
Mussel 21	13.797	57.991	Fragment 3	9.355	20.946
Mussel 22	11.666	55.409	Fragment 1	12.503	29.829
Mussel 23	10.928	54.579	Fragment 2	15.146	46.706
Mussel 24	14.071	63.708	Fragment 3	9.987	29.887

Table A.11. The ratios between the thickness d of the shells and the grain roughness k_s of the surface for the sample shells.

Sample	$\frac{d}{k_s}$ ratio		Sample	$\frac{d}{k_s}$ ratio	
	$D_{50} = 0.3\,\text{mm}$	$D_{50} = 0.9\,\text{mm}$		$D_{50} = 0.3\,\text{mm}$	$D_{50} = 0.9\,\text{mm}$
Mussel 1	3.3	1.1	Mussel 25	2.0	0.7
Mussel 2	3.3	1.1	Mussel 26	6.3	2.1
Mussel 3	3.3	1.1	Mussel 27	2.0	0.7
Mussel 4	3.2	1.1	Mussel 28	2.0	0.7
Mussel 5	3.3	1.1	Mussel 29	3.7	1.2
Mussel 6	3.3	1.1	Mussel 30	3.3	1.1
Mussel 7	3.2	1.1	Mussel 31	3.2	1.1
Mussel 8	3.0	1.0	Mussel 32	3.5	1.2
Mussel 9	3.0	1.0	Limpet 1	6.7	2.2
Mussel 10	3.0	1.0	Limpet 2	4.0	1.3
Mussel 11	3.0	1.0	Limpet 3	4.0	1.3
Mussel 12	3.0	1.0	Limpet 4	3.3	1.1
Mussel 13	2.7	0.9	Limpet 5	2.8	0.9
Mussel 14	3.0	1.0	Clam 1	5.0	1.7
Mussel 15	3.0	1.0	Clam 2	4.3	1.4
Mussel 16	3.0	1.0	Clam 3	3.3	1.1
Mussel 17	2.7	0.9	Clam 4	5.0	1.7
Mussel 18	2.3	0.8	Clam 5	3.3	1.1
Mussel 19	2.7	0.9	Fragment 1	3.3	1.1
Mussel 20	2.3	0.8	Fragment 2	1.7	0.6
Mussel 21	2.0	0.7	Fragment 3	0.7	0.2
Mussel 22	2.0	0.7	Fragment 1	1.7	0.6
Mussel 23	2.0	0.7	Fragment 2	3.3	1.1
Mussel 24	2.0	0.7	Fragment 3	0.7	0.2

References

[1] J. Dronkers. Dynamics of coastal systems. Advanced series on ocean engineering 25, 2005.

[2] J. Wright, A. Colling, and D. Park. *Waves, tides, and shallow-water processes*, volume 4. Gulf Professional Publishing, 1999.

[3] S. Dey. Incipient motion of bivalve shells on sand beds under flowing water. *Journal of engineering mechanics*, 129(2):232–240, 2003.

[4] Y.C. Ted. *Sediment Transport Theory and Practice*. McGraw-Hill, Singapore, 1996.

[5] R.C. Ramsdell, S. A. Miedema, and A.M. Talmon. Hydraulic transport of sand/shell mixtures. In *ASME 2011 30th International Conference on Ocean, Offshore and Arctic Engineering*, pages 533–547. American Society of Mechanical Engineers, 2011.

[6] V.A. Vanoni. Sedimentation engineering. *ASCE-manuals and reports on engineering practice (*, (54), 1975.

[7] G. Domokos, A. Sipos, T. Szabó, and P. Várkonyi. Pebbles, shapes, and equilibria. *Mathematical Geosciences*, 42(1):29–47, 2010.

[8] G.R. Alger and D.B. Simons. Fall velocity of irregular shaped particles. *Journal of the Hydraulics Division*, 1968.

[9] V. Te Chow. *Open channel hydraulics*. McGraw-Hill Book Company, Inc; New York, 1959.

[10] S. Montes. *Hydraulics of open channel flow*. American Society of Civil Engineers, Baltimore, MD (US), 1998.

[11] Z. Liu. Sediment transport. *Aalborg Universitet*, pages 54–56, 2001.

[12] H. Schlichting. *Boundary-layer theory.* McGraw-Hill, 1968.

[13] V. Méndez. *Sediment transport in irrigation canals.* UNESCO-IHE, Institute for Water Education, 1998.

[14] J.M. Francisco. Flow resistance in open channels with fixed and movable bed. In *2nd Joint Federal Interagency Conference, Las Vegas*, volume 27, 2010.

[15] N.S. Cheng. Revisited vanoni-brooks sidewall correction. *International Journal of Sediment Research*, 26(4):524–528, 2011.

[16] J. Kiijarvi. Darcy friction factor formulae in turbulent pipe flow. *Lunowa Fluid Mechanics Paper*, pages 1–11, 2011.

[17] H.A. Einstein. Formulas for the transportation of bed load. *Trans. ASCE Paper*, 2140:561–597, 1942.

[18] J. Johnson. The importance of side wall friction in bed-load investigation. *Proceeding Civil Engineering*, 12(6):339–331, 1942.

[19] J.N. Recicar, L.A. Pereira, and M.H Hirata. Harmonic oscillations of a circular cylinder moving with constant velocity in a quiescent fluid. In *11th Brazilian Congress of Thermal Sciences and Engineering, Proceedings of ENCIT*, pages 5–8, 2006.

[20] Y. Peysson, M. Ouriemi, M. Medale, P. Aussillous, and É. Guazzelli. Threshold for sediment erosion in pipe flow. *International Journal of Multiphase Flow*, 35(6):597–600, 2009.

[21] E.D. Andrews. Entrainment of gravel from naturally sorted riverbed material. *Geological Society of America Bulletin*, 94(10):1225–1231, 1983.

[22] N. Chien and Z. Wan. *Mechanics of sediment transport.* ASCE Press, USA, 1999.

[23] A. Shields. Application of similarity principles and turbulence research to bed-load movement. Technical report, Soil Conservation Service, 1936.